Mesoscale and Submesoscale Processes in the Southeast Atlantic and Their Impact on the Regional Thermohaline Structure

Tonia Astrid Capuano, Sabrina Speich, Xavier Carton, Bruno Blanke

To cite this version:

Tonia Astrid Capuano, Sabrina Speich, Xavier Carton, Bruno Blanke. Mesoscale and Submesoscale Processes in the Southeast Atlantic and Their Impact on the Regional Thermohaline Structure. Journal of Geophysical Research. Oceans, 2018, 123 (3), pp.1937-1961. 10.1002/2017JC013396 . hal-02107691

HAL Id: hal-02107691
https://hal.science/hal-02107691v1

Submitted on 22 Jun 2022

AGU PUBLICATIONS

JGR

Journal of Geophysical Research: Oceans

RESEARCH ARTICLE

10.1002/2017JC013396

Key Points:

- Mesoscale spatiotemporal variability in the Cape Basin is also influenced by submesoscale mechanisms
- Seasonality of the flow instabilities highly affects the dynamics of the upper and lower thermocline water masses
- Small-scale processes strongly impacts the Indo-Atlantic transports of heat and salt

Supporting Information:

- Supporting Information S1
- Figure S1
- Figure S2
- Figure S4

Correspondence to:
S. Speich,
speich@lmd.ens.fr

Citation:
Capuano, T. A., Speich, S., Carton, X., & Blanke, B. (2018). Mesoscale and submesoscale processes in the Southeast Atlantic and their impact on the regional thermohaline structure. *Journal of Geophysical Research: Oceans*, *123*, 1937–1961. https://doi.org/10.1002/2017JC013396

Received 29 AUG 2017
Accepted 13 JAN 2018
Accepted article online 22 FEB 2018
Published online 12 MAR 2018

Mesoscale and Submesoscale Processes in the Southeast Atlantic and Their Impact on the Regional Thermohaline Structure

Tonia Astrid Capuano[1], **Sabrina Speich**[2], **Xavier Carton**[1], **and Bruno Blanke**[1]

[1]LOPS-UBO, Laboratoire d'Oceanographie Physique et Spatiale, Brest, France, [2]Laboratoire de Meteorologie Dynamique, LMD-IPSL, Ecole Normale Superieure, Paris, France

Abstract The turbulent processes in the Cape Basin, the southeasternmost gate of the Atlantic Ocean, play a key role in the transport and mixing of upper to intermediate water masses entering the area from the Indian Ocean, making them especially relevant for the Indo-Atlantic transfer of heat and salt. In this paper, two numerical simulations at different horizontal resolutions are used to study mesoscale and submesoscale dynamics, their phenomenology, their evolution, and their impact on the local water masses. Submesoscale processes seasonally affect both, the upper and intermediate layers, but there are clear dynamical differences between the two layers. Several types of instabilities underline this spatial and temporal variability. Near the surface, mixed layer instabilities occur during winter, while mesoscale-driven instabilities, as the symmetric type, prevail in summer. The connection between these two seasonal regimes is ensured, in anticyclonic eddies and within the mixed layers, by Charney baroclinic instabilities, involved in the local formation and subduction of mode water, that we have dubbed as Agulhas Rings mode water. Intermediate depths are instead characterized by mesoscale mechanisms of density compensation and lateral stirring of the tracer variance, triggering a significant filamentogenesis whose vertical scales are comparable to those mentioned in previous studies. This leads to a particularly efficient mixing of Antarctic Intermediate Waters of Indian and Atlantic origins. Lagrangian estimates highlight the new and significant role of fine scale structures in setting the water masses properties of upper and lower thermocline waters materializing the Indo-Atlantic exchange and therefore potentially affecting the global ocean circulation.

1. Introduction

1.1. The Indo-Atlantic Interocean Exchange

The Agulhas Current (AC) is the western boundary current of the southern Indian Ocean subtropical gyre and is primarily driven by the large-scale pattern of wind stress curl between the southeast trade winds and the Southern Hemisphere westerlies (Beal et al., 2011). South of the Agulhas Bank, at the outer edge of the continental shelf, the AC retroflects sharply, and continues eastward as the Agulhas Return Current (ARC; Lutjeharms et al., 1992). At the Agulhas Retroflection (AR), the current regularly loops back upon itself, and large anticyclonic eddies (known as "Agulhas rings") are shed in the Cape Basin, and, from there, they move into the South-Atlantic Ocean (Lutjeharms & Gordon, 1987; Ou & de Ruijter, 1986).

The transport of water from the South-Indian to the South-Atlantic oceans has substantial implications for the convective circulation of the Atlantic Ocean as a whole (Gordon, 1985). Weijer et al. (1999) and Biastoch et al. (2008) have demonstrated that these interbasin fluxes of heat and salt are important for maintaining the strength and operation of the Atlantic Meridional Overturning Circulation (AMOC). Past descriptions of the Indo-Atlantic exchange suggested that this transport is mainly dominated by the migration of Agulhas rings from the AR through the Cape Basin into the western South-Atlantic (see Lutjeharms, 1996 for a summary of observational studies). Other numerical experiments have focused on the turbulent activity of this oceanic basin (Biastoch et al., 2008; Drijfhout et al., 2001; Matano & Beier, 2003; Reason, 2001; Treguier et al., 2003; You et al., 2003), underlining how Agulhas eddies influence not only the transient transports but also fluxes associated with the mean circulation (eddy fluxes, for example, supply most of the energy of the Benguela Current; Veitch et al., 2009).

In particular, the work of Matano and Beier (2003) indicated that a distinctive characteristic of the eddy variability within the Cape Basin is the coexistence of cyclonic and anticyclonic vortices in dipole structures that resemble the Heton model (Hogg & Stommel, 1985). The same authors pointed out that the momentum fluxes, essential to the kinetic energy balance of the Cape Basin, are primarily driven by baroclinic and barotropic eddies, with negligible contributions from the mean circulation. In support to the latter, Lagrangian studies suggested that the transfer of properties and their mixing, rather than being uniformly distributed across the entire subtropical gyre, appears to be concentrated in some small regions (Boebel et al., 1998). The Cape Basin is one of them, characterized as the highest world ocean spot of eddy kinetic energy (Boebel et al., 2003). This implies that the mesoscale details of the interbasin exchanges are extremely important and cannot be simply represented by some constant mixing coefficient in diagnostic, large-scale, model simulations (Gordon et al., 1992).

In summary, the Indo-Atlantic interocean exchange is currently thought to consist of three major parts (De Ruijter et al., 1999; Lutjeharms, 1996): (1) the advection of Agulhas filaments, (2) the shedding of Agulhas rings (Lutjeharms et al., 1992), and (3) the transport and mixing of intermediate water between the two Southern Hemisphere subtropical gyres of the Indian and Atlantic Ocean (Rusciano et al., 2012; Speich & Arhan, 2007; Speich et al., 2007). Since the contribution of Agulhas filaments is thought to be significantly smaller than that of Agulhas rings (Schmid et al., 2003), this paper will mainly focus on the last two components of this exchange. Eddies of both signs are indeed fundamental for the advection of the local water masses and the transfer of the related T-S anomalies in the Cape Basin, as already suggested in earlier observational studies (Arhan et al., 2011; Boebel et al., 2003; Giulivi & Gordon, 2006; Lutjeharms et al., 2003). In this context, we will mainly focus on the analysis of anticyclones since they have a much longer lifetime than cyclones (Dencausse et al., 2010; Laxenaire et al., 2018) and also because the targeted instabilities at mesoscale are better resolved within the largest Agulhas rings detected in our simulated domain.

1.2. The Role of Agulhas Rings

Several studies, based on satellite-altimetry data, have led to a general agreement on the way Agulhas rings cross the South-Atlantic Ocean (Byrne et al., 1995; Gordon & Haxby, 1990; Laxenaire et al., 2018; Schouten et al., 2000). They showed that once these eddies have escaped the southeastern Cape Basin, they propagate north-westward as isolated structures at latitudes of 20°S–35°S, generally slowing down at the approach of bathymetric ridges. The Agulhas rings move partly due to β-induced motion and partly due to advection by the background currents (De Ruijter et al., 1999). Their speed and tracks are influenced by bottom topography and interaction with other eddies (Byrne et al., 1995; Laxenaire et al., 2018; Schouten et al., 2000). Ring translation speeds have been reported to vary between 3 and 16 km/d (Goni et al., 1997; McDonagh et al., 1999) and within 10 months after their formation most rings have reached the Walvis Ridge (Schouten et al., 2000). However, the behavior of Agulhas rings in the southeastern Cape Basin, closer to their formation region, is more complex, and was at times presented in contrasted manners.

Garzoli and Gordon (1996), Garzoli et al. (1996), and Goni et al. (1997), emphasizing the net north-westward translation of the rings in the Cape Basin, defined a relatively narrow ring corridor in which they would propagate and where Atlantic water from the west and Indian water from the east would mix. Boebel et al. (2003), on the other hand, stressed the attention on the turbulent character of the southeastern Cape Basin and the ensuing intense water mass mixing. Schouten et al. (2000) have pointed out that shear diffusion, due to small-scale dispersion and large-scale deformation of the rings, may be an important decay mechanism in the Cape Basin, together with convective modification and double diffusive interleaving. Overall, the shedding of large Agulhas eddies and rings certainly play a key role for the entrainment of Indian Ocean waters into the South Atlantic, even if it still remains unclear how these transient fluxes are ultimately driven into the North Atlantic basin (Treguier et al., 2003).

1.3. Cape Basin Water Masses

Hydrographic and tracer data show that the westward transfer of Indian Ocean water into the Southeast Atlantic is limited to waters with potential densities, with respect to the sea surface, lower than the 27.5 σ_{theta} isopycnal surface and shallower than 1,500–2,000 m (Gordon et al., 1992). The Indian water masses involved in this exchange are those advected by the Agulhas Current: South Indian Central Water, Subtropical mode water, Indian Antarctic Intermediate Water and, eventually, Red Sea Water. These waters meet and partially mix with Central and Intermediate waters of the South Atlantic as well as Subantarctic Surface Waters (Giulivi & Gordon, 2006; Gordon et al., 1992; Rusciano et al., 2012).

Recent studies have pointed out that the Cape Basin is a key region for the global MOC but also in terms of water masses modifications. This is partly due to the intense air-sea interactions that transform the upper Indian Ocean water core of Agulhas Rings, made of South Indian Central Waters and Subtropical mode waters, in different varieties of what we can call Agulhas Rings "Mode Water" (ARMW). The latter are characterized by homogeneous layers 200–600 m thick and potential densities varying from 26.0 to 26.8 σ_{theta} (Arhan et al., 1999, 2011; Gladyshev et al., 2008). While ARMW has been accounted from in situ data, ocean models are unable to represent it: modeled Agulhas Rings are characterized by a stably stratified structure (Rimaud et al., 2012).

Another important water mass that takes part in the Indo-Atlantic exchange and is modified in the Cape Basin is Antarctic Intermediate Water (AAIW). In this region, the fresh South Atlantic AAIW (A-AAIW) converges with the saltier and older Indian AAIW (I-AAIW; Jacobs & Georgi, 1977). Their mixing gives rise to the Indo-Atlantic AAIW (IA-AAIW) having an intermediate minimum value of salinity (Rusciano et al., 2012), and this happens isopycnally as I-AAIW and A-AAIW have comparable densities (27.2 σ_{theta}). It has been observed that I-AAIW advected in the Cape Basin within Agulhas Rings undergoes to modifications (freshening by mixing with A-AAIW) rapidly after the rings have entered our study region (Schmid et al., 2003). Again, numerical models are currently not able to realistically reproduce the physical processes driving this regional transformation of AAIW in the ocean interior (Rimaud et al., 2012). Hence, they do not simulate correctly the transport and properties fluxes into the South Atlantic associated with these water masses (Rimaud et al., 2012).

1.4. Objectives and Outline of the Study

In the present work, we will mainly focus on the 3-D structure, variability, and dynamical characteristics of the Cape Basin mesoscale eddies, with a particular emphasis on anticyclones. In parallel, we will numerically explore the nature and origin of submesoscale processes and diagnose the different types of instabilities that may derive from them. An additional goal of this study will be to assess the impact of these mesoscale and submesoscale processes on the dynamics and on the formation and transformation of the upper 1,500 m water masses, in order to better understand their role in the Indo-Atlantic interocean exchange.

In light of the above mentioned objectives, the paper is organized as follows. In section 2, the numerical framework is described: the model setup is briefly presented and some technical characteristics of the two analyzed configurations are provided. In this section, we also introduce the diagnostics used to investigate the different types of instabilities that could characterize the interactions between the mesoscales and submesoscales. The principal differences between the horizontal resolutions of the two simulations are presented in section 3, principally in terms of energetics. This section closes up with a discussion on the emerging evidence of a separation, in distinct dynamical regimes, between the upper layers and those at intermediate depths, at the base of the thermocline. Section 4 focuses on the turbulent activity within the upper layers: the instabilities at play, the energy transfers associated with them and the seasonality of the interactions between the mesoscale and submesoscale. An assessment of the impact of these turbulent structures on the thermohaline properties of the local mode waters is also presented at the end of this section, where we address the possible occurrence of Charney baroclinic instabilities (C-BCIs) within the mixed layer and their implication in the formation and subduction of a local variety of mode waters (ARMW), as we have previously defined them. In section 5, we first provide some general remarks on the effects of the density-compensation mechanism on AAIW dynamics and then discuss the plausibility that the mesoscale stirring of tracers is responsible for mixing different types of AAIWs within the Cape Basin. Lastly, in section 6 we present preliminary Lagrangian results on the role played by small-scale processes in the Indo-Atlantic exchange of thermocline waters, before offering a summary of the main results, together with some prospectives and conclusions of this work, in section 7.

2. Methods

2.1. The Numerical Model

The study is carried out using the IRD-UCLA version of the Regional Ocean Modeling System (ROMS; Shchepetkin & McWilliams, 2003, 2005), which has been extensively and successfully tested in the Cape

Basin region (Rimaud et al., 2012; Rubio et al., 2009; Speich et al., 2006; Veitch et al., 2009). This circulation model is a split-explicit and free-surface model that makes the Boussinesq and hydrostatic assumptions when solving the primitive equations. The code uses a third-order upstream biased scheme for advection, which provides lateral diffusivity/viscosity (Shchepetkin & McWilliams, 2009).

In the vertical, the model is discretized on a sigma, or topography-following, stretched coordinate system. The grid is isotropic and does not introduce any asymmetry in the horizontal dissipation of turbulence, allowing a fair representation of mesoscale dynamics (Penven et al., 2006). The bottom topography is derived from the ETOPO2 (2 arc-min resolution) database (Smith & Sandwell, 1997). Although the latest version of the model includes a pressure gradient scheme associated with a specific equation of state to limit errors in the computation of the pressure gradient (Shchepetkin & McWilliams, 2009), the bathymetry has been filtered in order to keep the "slope parameter" $r < 0.25$. The model has 100 vertical levels and the vertical sigma-coordinate is homogeneously distributed along the water column. In our configurations, we also activated the optimizing function of the vertical coordinate system that ensures an increased resolution in the subsurface and a fair smoothing of the tracer fields (Lemarie et al., 2012). This numerical choice has shown to be very influential for a "realistic" representation of the water masses characteristics of our study region.

All the model external forcing functions are derived from climatologies. At the surface, the model heat and fresh water fluxes are extracted from the COADS climatology (Da Silva et al., 1994). The initial condition of the model is an ocean at rest with temperature and salinities from the World Ocean Atlas (WOA) for the month of January. For the wind stress, a monthly mean climatology is computed from QuikSCAT scatterometer data (Ayina et al., 2006; Bentamy et al., 2003). The deliberate choice of using a climatological wind forcing for a simulation that is forced for multiple years is in accordance with the focus on equilibrium dynamics. Moreover, it allows for an investigation of intrinsic, or unforced, system variability. At the four lateral boundaries an active, implicit, upstream-biased, radiation condition (Marchesiello et al., 2001) connects the model solution to the monthly means of forcings extracted from the WOA climatology. The vertical mixing scheme is based on the K-profile parametrization (KPP) of Large et al. (1994), while the horizontal mixing is parametrized as a linear combination of Laplacian and biharmonic mixing, scaled with the grid size (Lemarie et al., 2012).

Our model is integrated for 5 years and the output fields are stored and daily averaged every day. Two horizontal resolutions are set: a high-resolution simulation (AGU12_36_108) at 1/12° horizontal resolution nested with a 1/36° and 1/108°, that is fully mesoscale and submesoscale resolving; and a medium-resolution simulation (AGU24_100_H) at 1/24° horizontal resolution, that partly permits submesoscale dynamics, but completely resolves mesoscale features. Results presented in this paper come from the analysis of the last 4 years of each simulation. The first year is discarded as a spin-up period required to reach statistical equilibrium and for eddy kinetic energy ($\mathrm{EKE} = 1/2\ ((u_{std})^2 + (v_{std})^2)$, where u and v are the zonal and meridional velocity components, and "std" designates the standard deviation of their instantaneous values) to reach a plateau. In these two simulations, we also make use of the tracking methodology of Chaigneau et al. (2008) to detect eddies for: discriminating between anticyclones (ACes) and cyclones (Ces); tracing their contours over horizontal maps; and localizing their centers for computing specific diagnostics.

2.2. The Two Model Configurations

Analysis of the high-resolution simulation and comparison between the two simulations allow us to isolate processes that are directly linked to submesoscales. But before proceeding in this direction, we briefly present each of the two simulations. Our lowest resolution simulation, AGU24_100_H, is a fully mesoscale-resolving, submesoscale-permitting configuration, characterized by a horizontal grid-spacing, Δx, equal to $\sim$3.6 km and 100 sigma-levels, homogeneously distributed, in the vertical. Our highest resolution solution, AGU12_36_108, consists of a double-way nested configuration with two child grids embedded within a parent domain (Figure 1a). The latter represents a 1/12° ($\Delta x \simeq 8$ km) run with 100, homogeneously distributed, vertical levels, forcing a first child domain at 1/36° ($\Delta x \simeq 2.7$ km), placed just after the Agulhas Retroflection and, embedded into it, a second child domain at 1/108° ($\Delta x \simeq 0.8$ km), centered on the area of the Cape Basin. Figure 1a shows the geographical extensions of the three domains of our nested solution. This simulation employs the two-way AGRIF embedding capability of ROMS (Debreu & Mazauric, 2006), which is designed such that the output from the lower resolution parent domain provides boundary conditions for

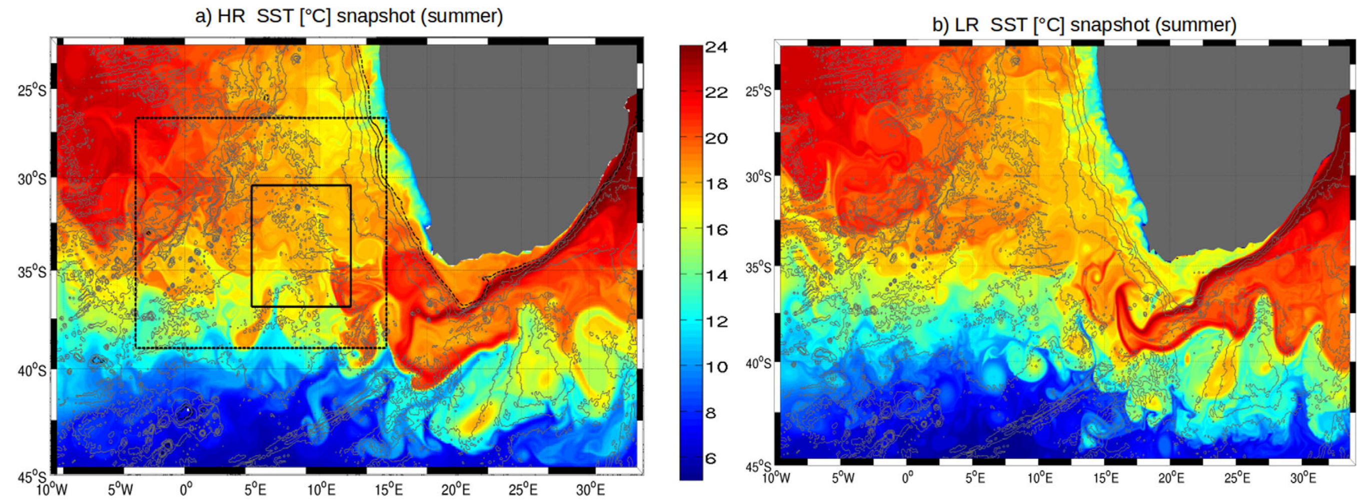

Figure 1. Instantaneous maps of Sea Surface Temperature (SST [°C]) showing the geographical extensions of the two numerical simulations analyzed in this paper: (a) the three domains of the nested, HR solution and (b) the one of the mesoscale-resolving, LR simulation. Black contours are for the −5,000, −4,000, −3,000, −2,000, −1,000, −500, −200, and −100 m isobaths from the Etopo2 data set (Smith & Sandwell, 1997).

the higher resolution child domains nested within it and the child domains in turn feed the parent domain. This technique allows for more consistent boundary conditions and is far less costly than running the parent domain at the resolution of either one of the two child domains. The parent domain has exactly the same extension of the one covered by AGU24_100_H (Figure 1b), going from 10°W to 34°E and from 22°S to 45°S; the one of the first child is placed just after that the AC curls back eastward, spawning its rings westward (26°S–38°S, 3°W–15°E). The second child is then centered on the Cape Basin (30°S–37°S, 5°E–12°E), in an area intentionally chosen to be weakly affected by the complex topography of this region, in order to better isolate those physical processes directly related to the intrinsic ocean dynamics. As previously mentioned, all the simulations presented here are based on the same depth data set, parameters, and forcing. Hereafter we will refer to the nested and higher resolution simulation (AGU12_36_108) as HR (for high resolution), and to the lower resolution one (AGU24_100_H) as LR.

2.3. Diagnostics for the Instabilities Analysis

The submesoscale regime is characterized by the ability to transfer energy from the available potential energy (APE) and the KE of the mesoscale to smaller scales, opening the road toward the dissipative scales (McWilliams, 2008; Molemaker et al., 2010). Thus, we will primarily focus on the EKE release from different types of instabilities that can occur once ocean fronts intensify (Haine & Marshall, 1998). The first type we will consider is the general class of baroclinic MLIs, and we propose to quantify them through their direct expression, i.e., the conversion rate of APE to EKE (Boccaletti et al., 2007; Capet et al., 2008b; Fox-Kemper et al., 2008). This conversion is common to all baroclinic instabilities and can be evaluated in terms of eddy vertical buoyancy flux (VBF):

$$\mathrm{VBF} = < W'b' > \tag{1}$$

where W is the vertical velocity and b the buoyancy anomaly ($b = -(g/\rho_0)\rho$), while brackets denote a time average and the prime denotes fluctuations relative to this average. Then we quantify the conversion from mean KE (MKE) to EKE due the horizontal and vertical shear (HRS and VRS), calculated following the mathematical expressions given in Gula et al. (2015):

$$\mathrm{HRS} = - < u'u' > \frac{\partial < u >}{\partial x} - < u'v' > \left[\frac{\partial < u >}{\partial y} + \frac{\partial < v >}{\partial x}\right] - < v'v' > \frac{\partial < v >}{\partial y} \tag{2}$$

$$\mathrm{VRS} = - < u'w' > \frac{\partial < u >}{\partial z} - < v'w' > \frac{\partial < v >}{\partial z} \tag{3}$$

These diagnostics quantify the horizontal and vertical exchange of KE between the MKE and EKE components. In particular, a conversion of MKE to EKE ($\mathrm{HRS} > 0$) may be interpreted as representing barotropic instability. Conversely, if there is a nonlinear exchange from EKE to MKE ($\text{HRS} < 0$), the eddies act to strengthen the mean flow (Wells et al., 2000). Positive values of VRS could instead indicate the presence of Kelvin-Helmholtz instabilities. The predominance of one of the two source terms, VBF or $\text{HRS} > 0$, indicates that the eddy generation mechanism is primarily a baroclinic instability ($\text{VBF} > 0$) or a barotropic instability ($\text{HRS} > 0$).

The Okubo-Weiss (OW) is a metric used to identify elliptic (vorticity-dominated) and hyperbolic (strain-dominated) regions, which has been often applied to 2-D or quasi-geostrophic, quasi-non-divergent flows (Okubo, 1970; Weiss, 1991). For the general case of a nonnull horizontal divergence field, OW can be written as

$$\text{OW} = \sigma^2 - \omega^2 \tag{4}$$

where $\sigma = (\sigma_n^2 + \sigma_s^2)^{1/2}$ is the strain rate of the horizontal (u, v) velocity field, with its normal, $\sigma_n = \frac{\partial u}{\partial x} - \frac{\partial v}{\partial y}$, and shear, $\sigma_s = \frac{\partial u}{\partial y} + \frac{\partial v}{\partial x}$, components, and where $\omega = \frac{\partial v}{\partial x} - \frac{\partial u}{\partial y}$ is the vertical component of relative vorticity (RV). For positive values of OW, the strain prevails, whereas negative values correspond to a dominant vorticity-based dynamics, usually associated with vortex cores. This parameter can be used to characterize regions of concentrated vorticity, and thus of coherent eddies, in a given two-dimensional velocity field.

The structure and evolution of the Ertel potential vorticity (Q; Ertel, 1942) can be used as a means to help interpreting submesoscale physics, since their dynamics are intimately linked with processes that modify the potential vorticity (PV) field, such as the forcing by wind stress, the buoyancy fluxes and the advection of PV by eddies (Thomas, 2005). The mathematical form we have used here comes from Peliz et al. (2014):

$$Q = -\frac{1}{\rho}\left((f+\omega)\frac{\partial \rho}{\partial z} - \left(\frac{\partial v}{\partial z}\frac{\partial \rho}{\partial x}\right) + \left(\frac{\partial u}{\partial z}\frac{\partial \rho}{\partial y}\right)\right) \tag{5}$$

When Q is multiplied by the Coriolis parameter ($f = 2\Omega \sin \phi$), we theoretically expect negative values to appear in regions where symmetric instabilities could be at play, corresponding as well to areas where the gradient Richardson number (Ri) is <1. Ri can be defined as follows (Thomas et al., 2016):

$$Ri = \frac{N^2}{S^2} \tag{6}$$

where $N^2 = \frac{\partial b}{\partial z}$ and $S^2 = \frac{\partial u}{\partial z}^2 + \frac{\partial v}{\partial z}^2$. N^2 is the stratification and S^2 is the squared shear. According to theory, a stratified, actively mixing boundary layer (i.e., here in summer) with Ri close to 1 is consistent with fronts that are symmetrically unstable (Thomas et al., 2013), whereas for values less than 0.25 Kelvin-Helmholtz instabilities could be expected (Bruggemann & Eden, 2015). In section 4.2, we will verify the first possibility by analyzing surface maps and vertical sections of these three diagnostics for the two model resolutions.

A last diagnostic used to quantify the turbulence due to submesoscales and hence discriminate the capability of our two numerical resolutions to resolve them consists in estimating the frontogenetic tendency. Frontogenetic activity mostly develops near the ocean surface, where the absence of vertical velocities allows straining from mesoscale eddies to increase density variance, thus leading to an effective sharpening of existing density fronts (Lapeyre et al., 2006; McWilliams & Molemaker, 2011). Frontogenesis is commonly studied in terms of the frontal tendency function F_{sh} and we make use of its definition by Giordani and Caniaux (2001):

$$F_{sh} = -\overline{<\left(\frac{\partial \rho}{\partial x}\right)^2 \frac{\partial u}{\partial x} + \left(\frac{\partial \rho}{\partial y}\right)^2 \frac{\partial v}{\partial y} + \frac{\partial \rho}{\partial x}\frac{\partial \rho}{\partial y}\left(\frac{\partial u}{\partial y} + \frac{\partial v}{\partial x}\right) >} \tag{7}$$

where potential density ρ is related to buoyancy b, as seen in the VBF definition (equation 1). A positive sign of F_{sh} represents an increase in the magnitude of the density gradient (i.e., frontogenesis), while a negative sign indicates frontolysis or weakening of this density gradient.

In section 5.1, devoted to the processes of AAIW density compensation, we calculated the spiciness, here defined as in Smith and Ferrari (2009):

$$\gamma = \beta_t(T - T_0) + \beta_s(S - S_0) \tag{8}$$

where β_t and β_s respectively represent the coefficients of thermal expansion and haline contraction and T_0 and S_0 are reference values of temperature and salinity. Being spiceness a measure of the passive spatial variations of water mass properties in density units, the net discrepancy between its spatial variability in HR and LR will highlight how the two resolutions reproduce a very dissimilar type of lateral mixing.

3. Energetics

3.1. Horizontal and Vertical Submesoscale Signature

Before proceeding to the analysis of the diagnostics presented above, we will examine the differences between the two numerical experiments and the impacts that the small-scale features present in the high-resolution solution have on the simulated energetics. We first calculated the total KE spectra within the second child domain of HR, at different depths (near surface -5, -100, 500, and 800 m), by taking the instantaneous values of horizontal velocities and averaging them by season. In Figure 2, we show the spectra extracted for the summer (model year 5, month 1; i.e., Y5M1, Figure 2a) and winter (Y5M8, Figure 2b) seasons.

For both seasons, the spectral curves of HR (continuous line in all the curves of Figure 2) exhibit, at all depths, very energetic small-scales. In winter the spectral curve has, near the surface, a typical slope of k^{-2}, in agreement with previous findings on the submesoscales cascade of energy (Capet et al., 2008a; Klein et al., 2008). The curves at intermediate depths (500 and 800 m, cyan and magenta, continuous lines in Figure 2) present a slope close to -3 and show a weaker seasonal variability compared to the upper layers curves (red and blue, continuous lines in Figure 2), indicating how the dynamics of these intermediate layers are less affected by the seasonality of the surface forcing. The spectral curves of LR (dashed line in all the curves of Figure 2) have a slope close to -3 both in summer and winter, showing a negligible, seasonal difference at all depths, and a lack of submesoscale processes.

We use the vertical profiles of the root-mean-square (rms) of W for each resolution as a diagnostic to further discriminate the two simulations analyzed in this manuscript. Following the methodology detailed in Capet et al. (2008a), we decompose the total field into the temporal mean (W_{mean}), mesoscale (W_{ME}) and submesoscale (W_{SME}) components: $W_{Total} = W_{mean} + W_{ME} + W_{SME}$, in order to highlight the vertical contribution of the simulated, different spatial structures.

The horizontal spatial rms metrics were computed at each sigma-level, and then temporally averaged over the summer (Figure 3a) and winter (Figure 3b). Given our focus on the water mass dynamics of the upper to intermediate depth layers, without considering the impact of topographic effects, results are plotted here

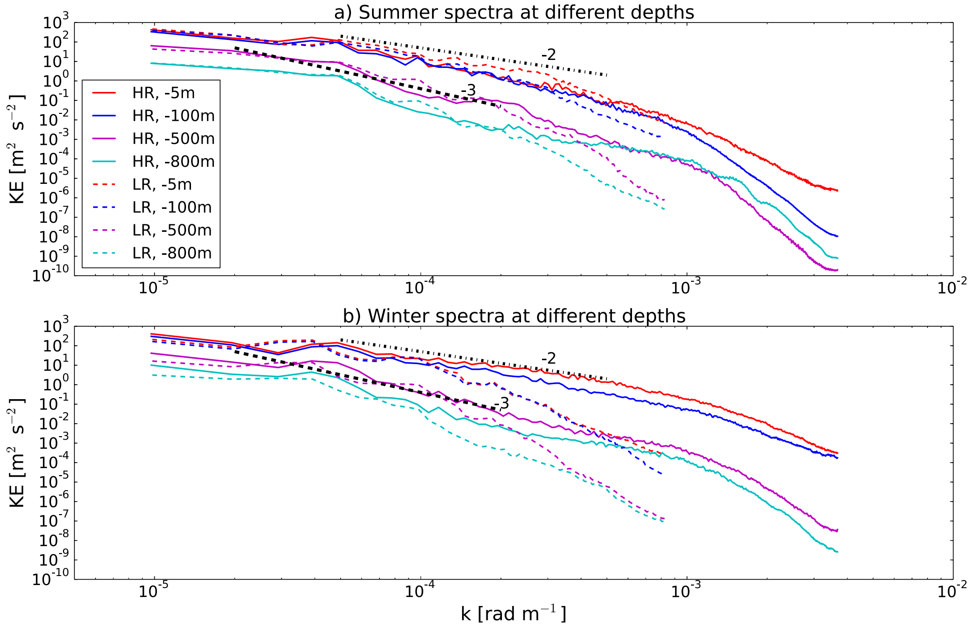

Figure 2. Kinetic Energy (KE) spectra computed at different depths from instantaneous values of horizontal velocities for the HR (continuous lines) and the LR (dashed) and averaged over (a) summer and (b) winter.

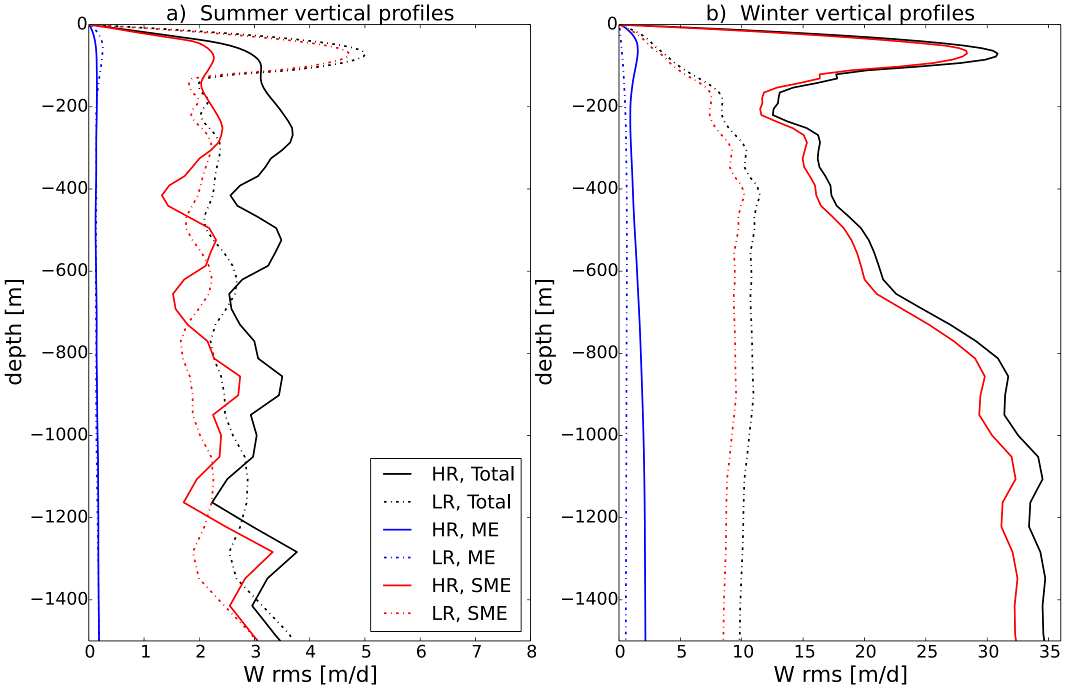

Figure 3. Root-mean-square (rms) profiles of the different components (total, mesoscale and submesoscale) of vertical velocity (*W [m/d]*), extracted in (a) summer and (b) winter along the first 1,500 m of the water column, for the HR (continuous lines) and the LR (dashed lines) simulations.

from the surface down to 1,500 m. The HR rms profiles of *W* present the most elevated magnitudes, where the total W_{rms} (i.e., $W_{rms}=\sqrt{<W^2>}$) is 4-fold higher than the LR profile in summer and up to 20-fold higher in its winter maximum peaks. This increase in magnitude is particularly significant in the submesoscale component of the velocity field, which is strongly enhanced close to the surface at both seasons. The surface signature is dominated by submesoscale activity, while mesoscale-induced vertical velocities are almost independent of depth. On the other hand, the submesoscale component in LR shows only minimal surface enhancement in winter, even if it intensifies in summer. At both resolutions the mesoscale and the submesoscale velocities are similar in structure, although the magnitudes are larger at HR, as it will be further investigated looking at vertical sections of VRS and VBF in section 4.1. Another important difference between the two simulations is the marked seasonal variability of all the W_{rms} components of HR, showing a dramatic change with seasons. In particular, the submesoscales winter values for HR are almost one order of magnitude higher than the summer ones, while only a negligible variation can be perceived for LR. We have observed, in experiments preparatory to this study (results not shown), that our model captures a seasonal cycle at increasing horizontal resolution. This seasonality will be explored in more details in section 4.3, by analyzing the seasonal behavior of the mixed layer depth (MLD) as reproduced in each of the two simulations.

3.2. Vertical Distinction of Dynamical Regimes

In Figure 4, we present zonal sections of temperature (*T*, Figure 4a), salinity (*S*, Figure 4b), potential density (σ_{theta}, Figure 4c), and meridional velocity (*v*, Figure 4d) of HR at Y5M1. They show the presence of an Agulhas ring between 7.5°E and 11°E, and also a layering of very different water masses between the surface and the intermediate depths. At the surface, a shallow mixed layer caps, within the Agulhas ring, a homogeneous layer of ARMW 300 m thick. At greater depth, we note an intense stratification above the AAIW layer, characterized by a salinity minimum, and a quasi-homogeneous layer, centered between 700 and 1,200 m and extending between the 27 and 27.4 isopycnals, with higher values of salinity (i.e., compared to the environment) found at the vertical of the eddy core.

Given the differences seen in the vertical distributions of *W* and *v* (respectively Figures 3b and 4d) between the upper layers (i.e., from the surface to the base of the mixed layer) and the AAIW depths of our study

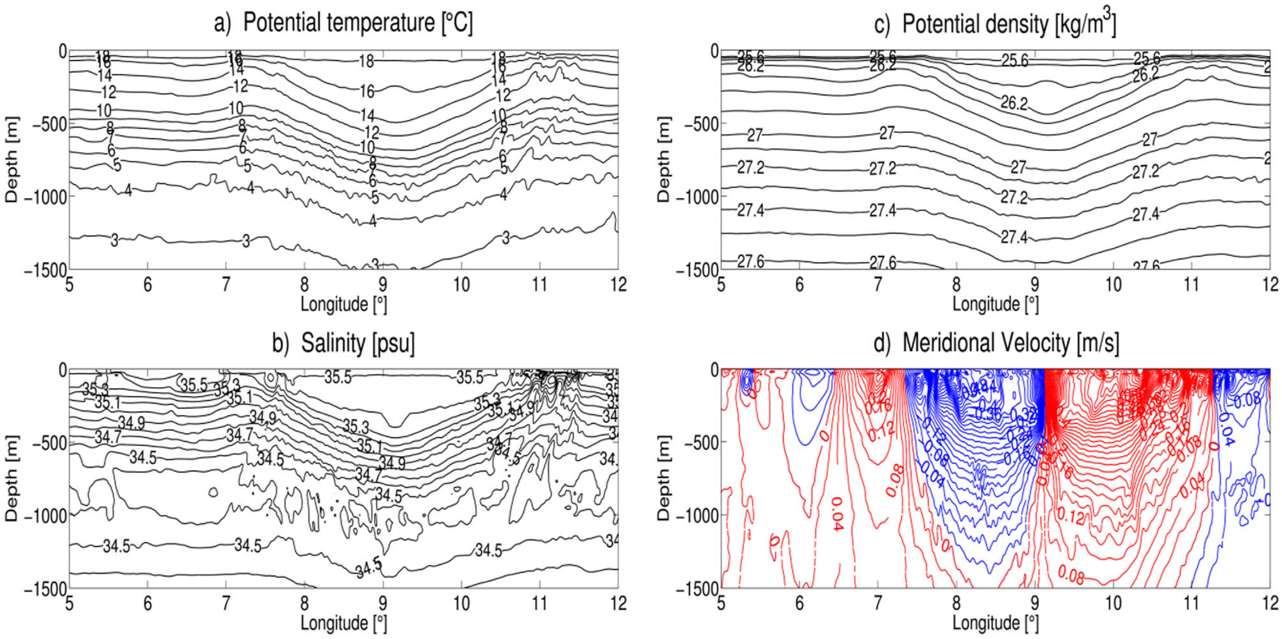

Figure 4. Zonal, instantaneous sections of (a) temperature [°C], (b) salinity [*psu*], (c) potential density anomaly (σ_{theta}), and (d) meridional velocity (v [m/s]) plotted at 34°S along a summer anticyclone detected in the HR simulation. In Figure 4d, red contours are for positive values of velocity and blue for negative.

region, confirmed by the spectral results of Figure 2, we further investigate this vertical distinction in dynamical regimes. The meridional velocity exhibits, for instance, higher magnitudes in the upper layers than at greater depth, which could be due to the influence of the surface forcing more efficient in the near surface than at depth.

In this regard, the diagnostics presented in the following sections will support the hypothesis initially proposed by Boebel et al. (2003) on the coexistence of two dynamical regimes between the upper and the intermediate layers of the Cape Basin, describing a "stirring" regime near the surface and a "blender" regime at greater depth. This was proven to be true by the observational work of Rusciano et al. (2012) and the numerical study of Rimaud et al. (2012), where Lagrangian integration of particles showed how both the vertical mixing and lateral stirring of AAIWs within the Cape Basin lead to the formation of new varieties of this water mass. Our results will confirm their findings investigating the different instabilities and the meso-submesoscales interactions that play a key role as triggering mechanisms of these processes.

To do so, we first focus on the energetic signature discriminating the upper and intermediate layers of our study region, looking at vertical profiles of EKE, VBF (equation (1)) and frontogenetic tendency (F_{sh}, equation (6)), extracted by spatially and temporally averaging their seasonal values for the two simulations and seasons contrasted in this paper (Figures 5a–5c).

Looking at the profiles of Figure 5, LR (blue lines) exhibits, in comparison to the HR curves (red lines), minor seasonal fluctuations in terms of the VBF depth distribution (Figure 5b), and even smaller for F_{sh} (Figure 5c), while it shows greater seasonal variability in the EKE distributions (Figure 5a). The latter is indeed characterized at LR by higher values in summer than in winter, suggesting a predominance of mesoscale dynamics in our region of study during the former season, as visible also at HR. At certain depths ($\sim$50 m in summer and $\sim$250 m in winter), the EKE at LR is more important in magnitude than at HR (e.g., at the surface in winter and below, at about 250 m, in summer), probably due to the lack of finer scales instabilities able to modify and eventually drain the EKE reservoir of the flow as it occurs in HR.

Concerning the VBF vertical distribution, the two resolutions show a similar patterns for both seasons, even though the amplitude of HR values is considerably larger than for LR (respectively red and blue lines in Figure 5b), and this is particularly true in winter. During this season, we observe, for both resolutions, an enhancement in VBF just below the surface and a decrease just below the mean MLD and again an increase coincident with the MLD maximum. At greater depths, VBF decreases at both resolutions and in HR it

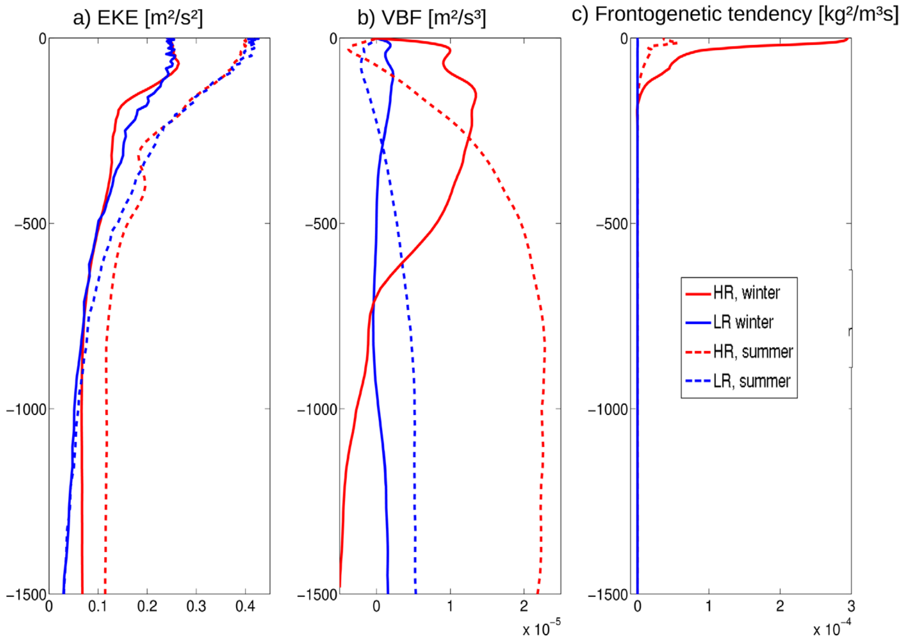

Figure 5. Vertical profiles of (a) Eddy Kinetic Energy (EKE), (b) vertical buoyancy flux (VBF), and (c) frontogenetic tendency (F_{sh}) for the HR (in red) and LR (in blue) simulations for summer (dashed lines) and winter (continuous).

becomes negative below 1,000 m. On the other hand, in summer at HR, the vertical maximum of VBF is reached at the level of the AAIW layer. Hence, this vertical distribution of VBF clearly underlines the separation between the dynamical regimes of the upper and intermediate layers.

The LR limits in resolving the presence of submesoscales and their seasonal intensification clearly emerge in the profiles of F_{sh} (Figure 5c), characterized by very low values, barely oscillating around the zero-baseline, for both seasons. The HR simulation shows, instead, considerable values of F_{sh} within the upper 300 m of the water column and they are particularly high in winter, being about one order of magnitude larger than in summer. This suggests that near-surface frontogenesis, likely resulting from the stirring of mean buoyancy gradients by the mesoscales, is in our region of study more active in winter, within a depth extending from the surface down to the ML base. We find that this layer could be also affected by C-BCIs and this possibility is more extensively discussed in the next section, where we separately present, for the upper and AAIW layers, specific diagnostics on the instabilities at play in each layer. For this analysis, we will restrict our discussion on the results obtained for two ACes, one for summer and one for winter, detected at HR and chosen as representative of the average, dynamical behavior of Agulhas Rings in the Cape Basin.

4. Upper Layers Dynamics

4.1. Mixed Layer Instabilities

Figures 3 and 5 have shown that the upper ocean dynamics at HR is dominated by an important submesoscale activity. We seek to understand its origin. First, we look for the occurrence of baroclinic MLIs, consisting of thermocline shear-driven instabilities that play a crucial part in the submesoscale dynamics of the surface ML (Boccaletti et al., 2007). To verify that our chosen ACes are generated through barotropic rather than baroclinic instabilities, we analyze the surface and vertical distributions of HRS (equation (2)), VRS (equation (3)), and VBF (equation (1)) for the summer and winter seasons (Figures 6a–6n). Positive and negative values are present at the two sides of the front localized along the eddy main axis, extending from 8°E to 9.5°E. Larger values of VBF are found in winter due to the more intense vertical velocities found in this season (Figure 3b), responsible for driving larger buoyancy fluxes. For the summer ACe, being geometrically close to an elliptic eddy with a Gaussian shape, we observe a quadripolar structure of HRS (Hua et al., 2013; Figure 6a), where the alternation of opposite sign values is related to the eddy deformation. The analyzed ACe is surrounded by two smaller Ces, exerting a shear on it and visible also in the HRS section (Figure 6g),

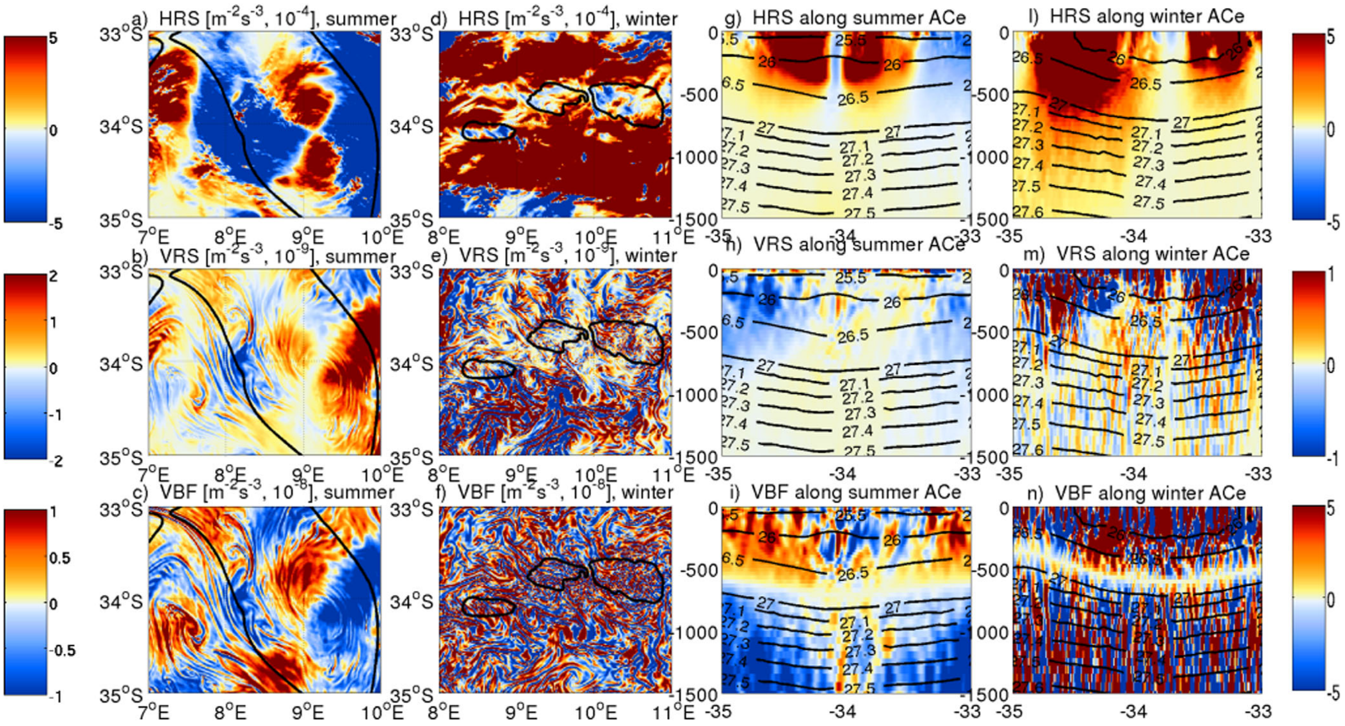

Figure 6. (left) Snapshots of horizontal and vertical shear (HRS and VRS [m^{-2} s^{-3}]) and vertical buoyancy flux (VBF [m^{-2} s^{-3}]) plotted along an ACe detected within the HR simulation in (left) summer and (right) winter. Black contours define the outer limits of the detected eddy. (right) Meridional sections of the same metrics, extracted at 9.2°E with black contours for isopycnals ranging from 26 to 28 σ_{theta}. Note that the maps of the left figure (a–f) share the colorbars on the left, while the ones on the right are for the sections of the right figure (g–n).

where the isopycnals doming and diving characterize the interacting eddies of opposite signs and mainly happen in summer.

In winter instead, the HRS surface map (Figure 6d) presents the highest positive values at the centers of the multiple, smaller vortices and filaments making up the ACe center (between 9.5°E and 10.5°E). Its spatial distribution is however much smoother than those of VRS and VBF (Figures 6e and 6f), strongly dominated by the occurrence of very fine scales, both within the contours of the ACe and at its surroundings. This suggests that weaker energy transfers due to the horizontal shear take place in winter, when submesoscales prevail, and that shear instabilities, like the barotropic ones, are mainly confined at the periphery of the summer eddies. Moreover, in the winter section of VBF (Figure 6n) the subduction of filaments, laterally generated by the shear between the ACe and the nearby Ces, indicates how the fine structures are mainly marked in VBF at depth, while more in HRS and VRS at the surface (Figures 6l and 6m).

Overall, VRS is more intense in winter than in summer, while HRS remains pronounced also in summer, even though more enhanced in winter, especially in terms of its vertical extension. VBF, in particular, shows a net contrast between the upper 300 m and the intermediate levels, being clearly separated by a layer in which VBF = 0, corresponding to the AAIW layer of low salinity (Figure 4b). This underlines the transition between the two different dynamical regimes (i.e., highly ageostrophic at the surface versus quasi-geostrophic at depth) introduced in section 3.3. We conclude this analysis by mentioning that the vertical separation between these two regimes is completely absent in the LR sections (not shown), where all the variables have a barotropic behavior at depth, confirming for LR a more diffusive dynamics.

4.2. Symmetric Instabilities

To assess if symmetric instabilities (Thomas et al., 2013, 2016) play a role in the simulated dynamics of the Cape Basin, we computed the OW parameter (equation (3)), the Ertel PV (Q, equation (4)) multiplied by the Coriolis parameter ($f \times Q$) and the gradient Richardson number (Ri, equation (5)). Figures 7a and 7d show two typical snapshots of OW extracted near the surface at both seasons for HR. The σ^2 term appears to be dominant in winter (positive OW), indicating a direct connection with the submesoscale field, since it

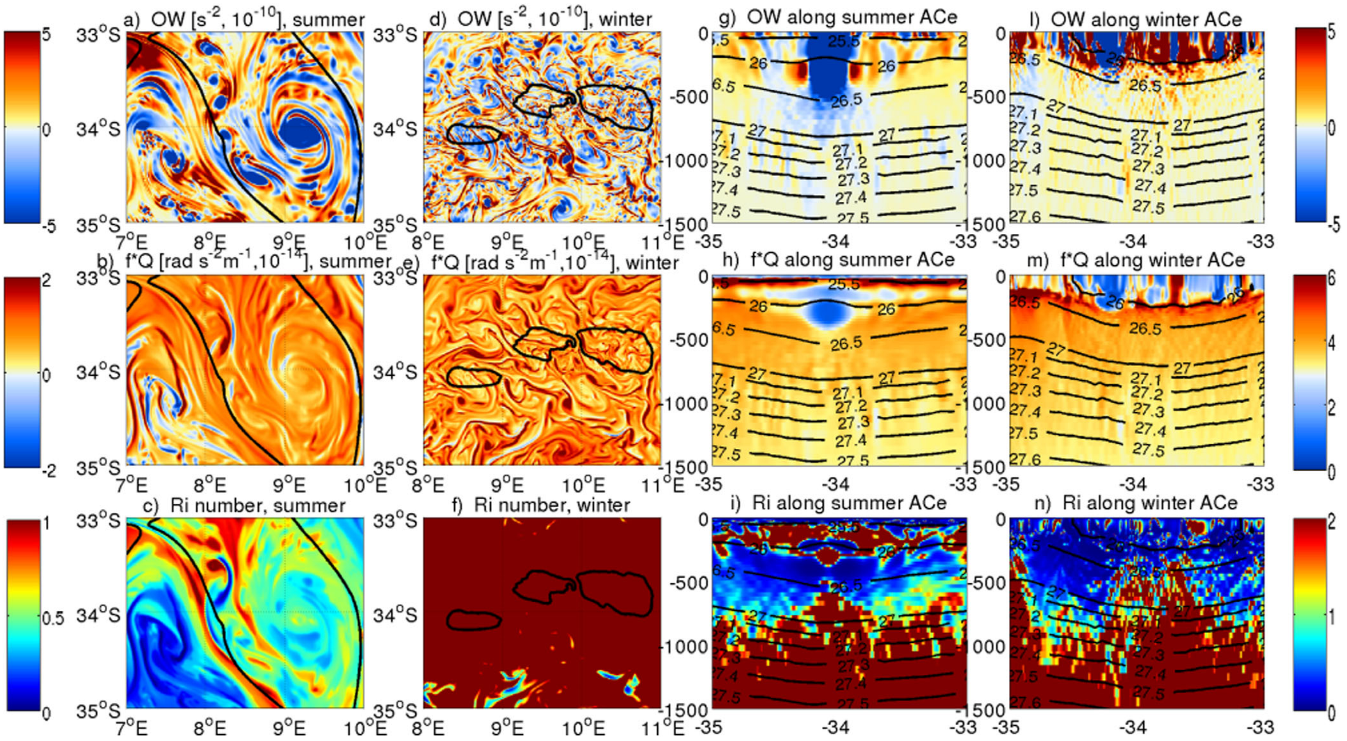

Figure 7. (left) Same as Figure 7 but showing the instantaneous maps of the Okubo-Weiss parameter (OW [s^{-2}]), the Ertel potential vorticity multiplied by the Coriolis parameter ($f \times Q$ [rad s^{-2} m^{-1}]) and the Richardson number (Ri). (right) Meridional sections of the same metrics, extracted at 9.2°E with black contours for isopycnals (26–28 σ_{theta}). Note that the maps of the left figure (a–f) share the colorbars on the left, while the ones on the right are for the sections of the right figure (g–n).

represents a signature not only of strain but also of divergence/convergence. The latter is strongly increased when frontogenesis and MLIs are more active (Mensa et al., 2013), as it happens during winter in our study region. The surface map of $f \times Q$ over the summer HR ACe (Figure 7b) shows filaments of negative values around the center of the eddy and at the periphery of it, corresponding to the same locations where $Ri < 1$ (Figure 7c). In LR (not shown here), filaments remain positive even when $Ri < 1$ (a necessary but not sufficient condition), confirming that LR is not able to capture the development of symmetric instabilities. As expected, at both resolutions the cores of the eddies are characterized by negative values of OW (Figures 7a and 7d).

In the summer sections of OW and $f \times Q$ (Figures 7d and 7e), we observe winter water isolation below the ML and the seasonal thermocline, identified by a core of negative values for these two variables. Here the eddy core is surrounded by filamentary structures, indicative of subduction (see section 4.4), as shown in an animation of PV and W sections, extracted at each time step from spring Y4M10- to the next summer-Y5M1- of our HR simulation (supporting information 1). These filaments are not well resolved by LR, neither are any of the other fine scales visible in the OW and $f \times Q$ maps of HR. Smaller vortices and filaments emerge in the winter maps of LR (not shown), even though they do not attain the HR fine scales (Figures 7d–7f), where the surface maps of the three quantities seem to be definitively dominated by the so-called "soup of submesoscales" (Capet et al., 2008a). The latter extends vertically down to 500 m of depth, and produces a thick, homogeneous band between the 26 and 26.5 isopycnals (Figures 7l–7n), creating a typical layer of mode waters within the Cape Basin, the ARMW. During winter, we observe in the upper layers fewer filaments where $f \times Q < 0$ and $Ri < 1$, suggesting that symmetric instabilities take place mostly in summer, in the HR simulation.

4.3. Seasonality of the Meso-Submesoscale Interactions

Overall, the regional dynamics in the Cape Basin is governed by mesoscale structures, triggering submesoscale instabilities in the shallow mixer layer, in summer, at the frontal edge of the mesoscale eddies. In winter smaller submesoscales, driven by the stronger atmospheric forcing, prevail and affect the entire region, and, in particular the interior of mesoscale eddies, extending from the surface to the deepest eddy layers. This is in agreement with the results initially shown in the KE spectra of Figure 2. In summer, the local dynamics is essentially characterized by mesoscale barotropic instabilities, leading to surface structures (filaments, fronts, and smaller vortices), whose interaction can trigger submesoscale shear instabilities, as the symmetric type. Instead, in winter, shallower baroclinic instabilities, like MLIs, forced by the action of the wind and the passage of seasonal storms, or induced by strong lateral gradients of density, dominate the upper layers. Below the thermocline, frontal instabilities develop during both seasons, due to the interaction between adjacent eddies of opposite signs, as observable in the animation of the PV and *W* sections (supporting information 1).

This indicates how the portion of submesoscales captured by HR is marked by a strong seasonality, as documented in previous numerical studies at comparable resolutions (Brannigan, 2016; Brannigan et al., 2015; Callies et al., 2015) and explained by the two main mechanisms identified by Callies et al. (2015). In summer, with a prevailing presence of mesoscale structures, submesoscale flows are energized by mesoscale-driven frontogenesis, where strain fields, at the edge of mesoscale eddies, sharpen surface buoyancy gradients. This clearly appears in the summer map of the OW surface distribution (Figure 7a), where the highest positive values, indicative of a strain predominance, can be found along submesoscale filaments and around the centers of the smaller vortices. Additionally, in the summer OW section (Figure 7g), we observe the density gradient sharpening at the edges of the core of the subsurface-intensified ACe, above which a thin layer of much finer scales develops close to the surface. These submesoscale flows are confined in the shallow surface layer, as shown in the VRS and VBF summer sections (Figures 6h and 6i), where very small scales are visible only in the first 50 m of the water column and correspond to the HR surface spectra of KE (Figure 2). From the same figure note also that the degree of geostrophic balance changes as the resolution increases with evidence for stronger, nonlinear processes becoming more important during the winter season, when the ML deepens (Brannigan et al., 2015). This is consistent with stronger instabilities developing within the ML as it thickens. They energize the submesoscales via baroclinic instability (the second mechanism of Callies et al. (2015), as was shown in the VBF surface map and vertical section for the winter ACe (Figures 6f and 6i). That is why HR, which reproduces a seasonal cycle, with a much thicker ML in winter than in summer and very pronounced compared to LR (see Table 1), captures the formation of such ML instabilities, as shown in the winter sections of OW and $f \times Q$ (Figures 7g and 7h). The MLD is here computed as the depth at which the density difference with respect to the surface is equivalent to a 0.03 density change.

Concerning its seasonal cycle, given that lateral buoyancy gradients are fairly constant throughout the year, the KE generated by fine-scale instabilities peaks in winter, when the ML is the deepest. In summer, with shallower ML, these instabilities are damped, as it appears from the HR horizontal and vertical distributions of energy transfers (Figure 6). Hence HR, resolving a portion of submesoscale processes, captures the nonlinear processes affecting the mixing layer and inducing a large seasonal variation that is not represented in LR (Table 1). This aspect will be further detailed in the next section.

4.4. Charney Baroclinic Instability and Mode Waters Subduction

Charney baroclinic instability (C-BCI; Charney, 1947) arises from the coexistence of a surface buoyancy gradient and an interior PV gradient, of opposite signs, and is able to couple the unstable evolutions of the ocean surface and interior, at mesoscale and submesoscale (Capet et al., 2016). A necessary and most frequently sufficient condition for C-BCI is that the vertical gradient of buoyancy frequency (dN^2/dz) changes sign (Charney, 1947). This can be achieved in layers of mode water (Capet et al., 2016), as those present in Agulhas rings (ARMW) and observed from in situ data to be located between the 26 and 26.8 isopycnals (Arhan et al., 1999, 2011; Gladyshev et al., 2008). Figure 4 shows that the lighter variety of ARMW (occupying the 25.8–26.2 isopycnals range) is well represented in HR (despite it experiences only a smooth winter forcing). The vertical seasonal distribution of dN^2/dz at HR reaches values of about -3, -4×10^{-7} s^{-2} m^{-1} and in some locations even lower than -5×10^{-7} s^{-2} m^{-1} (Figure 8), both in winter and summer ACes (Figures 9a and 9b, respectively).

Table 1
Table Listing the Mean Values of Mixed Layer Depth (MLD), Averaged Over the Summer and Winter Seasons Within All the Anticyclones, and Cyclones Detected in the HR Simulation and in the LR Solution

Mean MLD (m)	Summer	Winter
Aces	HR = 30	HR = 105
	LR = 36	LR = 54
Ces	HR = 30	HR = 107
	LR = 35	LR = 45

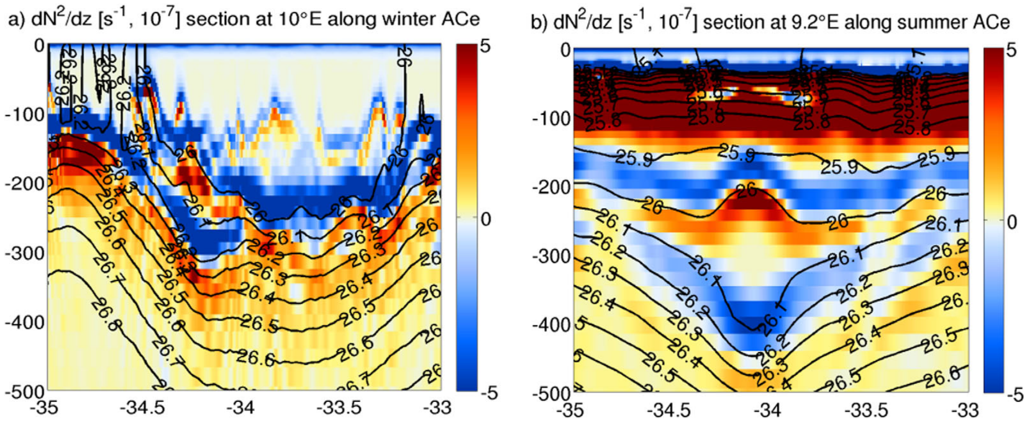

Figure 8. Meridional sections of the vertical gradient of stratification (dN^2/dz) plotted (a) at 10°E along a winter anticyclone and (b) at 9.2°E along a summer anticyclone for the first 500 m of the water column. Black contours are for isopycnals ranging from 25 to 26.8 σ_{theta}.

At places and times where mode waters are actively formed through convection, we expect more energetic instabilities (such as convective, symmetric, or MLIs) to dominate the upper ocean dynamics over a depth range comparable to that of negative dN^2/dz (Capet et al., 2016). The same authors hypothesize that C-BCI may impact mode water dynamics either through wintertime convection/subduction or due to calm weather conditions that render the surface mixed layer relatively shallow. Our case would rather be the first one since we observe hints of the ML subduction in the animation of the PV and *W* (supporting information 1). Meridionally and seasonally averaged profiles of *W* skewness also show in winter downward velocities greater than upward velocities in the near surface (supporting information 2).

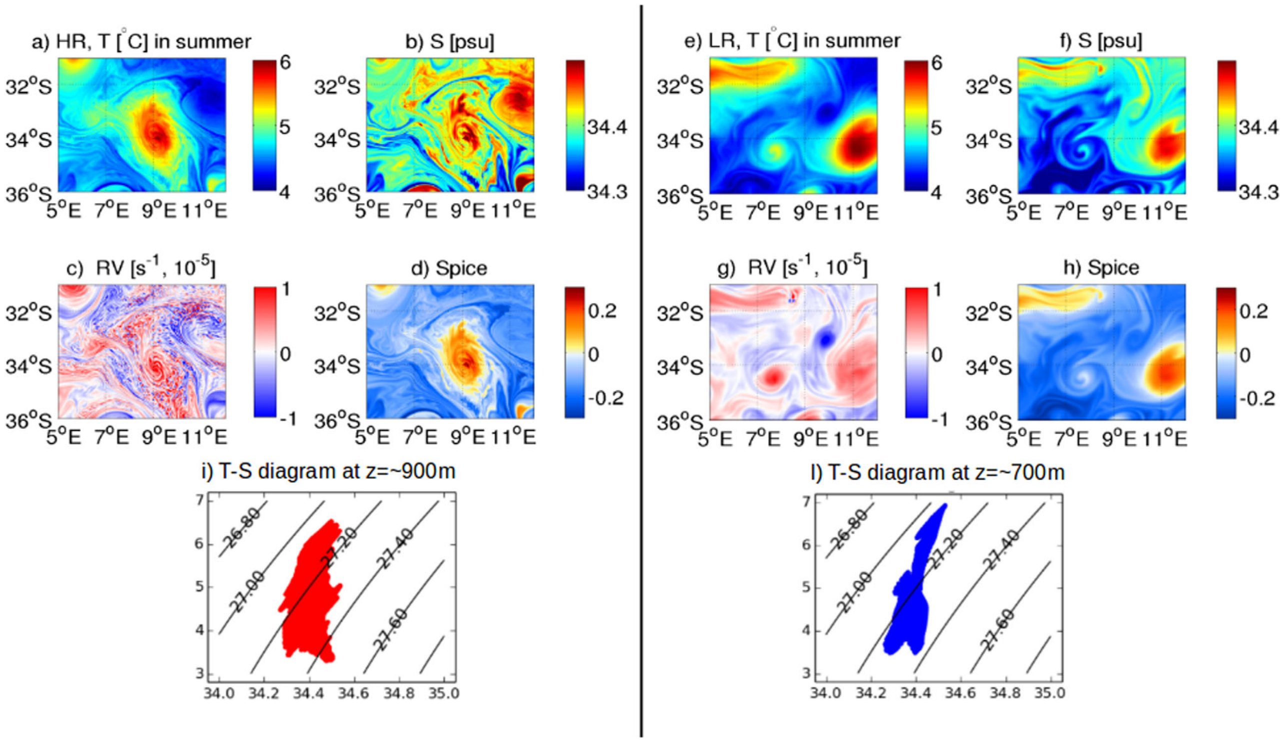

Figure 9. (top) Snapshots of temperature (*T*), salinity (*S*), relative vorticity (RV), and spice extracted along the 27.2 isopycnal over a summer ACe of (a–d) the HR and (e–h) the same for the LR. (bottom) Theta-S diagrams showing the same thermohaline distributions of the top figures, for HR (i) and the LR (l).

In our study region, the primary mechanism triggering subduction is likely frontogenesis, highly enhanced during winter in the upper 300 m of the water column (see the results for HR in Figure 6c). Subduction at upper ocean fronts is often driven by internal instabilities (mostly baroclinic, see Spall (1995)), where frontogenesis forces the water parcels below and across the front. Intense ageostrophic cross-front and vertical velocities (O(30 m/d), see Figure 3b for the HR winter profiles) may then take place, leading to the formation of deep ACes and shallow Ces during the subduction process. Here the subsurface-intensified ACes have their core below the ML base (see the dN^2/dz minimum in Figure 8), as seen in the HR summer sections of OW, $f \times Q$ and *Ri* (Figures 7d–7f). These ACes are mainly biconvex lenses, often axisymmetric, below which the isopycnals deflection, quantified by $d\rho/dz$, is of the order of 10^{-3} kg/m^4. An analysis of several model runs (not shown here) indicates that most of the simulated ACes are close to Gaussian in profile and elliptical in shape. Thus, HRS is quadripolar (Figure 6a), whose mode 2 deformation is due to the shear of neighboring currents and eddies (Hua et al., 2013). These elements support our interpretation that subduction is important in creating the minimum stratification layers conducting to C-BCIs at the mode waters depths.

To summarize, our results on the ARMW seasonal formation and subduction suggest that, in winter, the more intense atmospheric air-sea interactions deepen the MLD by destratifying the water column and enhancing frontogenesis within this layer. This leads to the generation of submesoscale internal instabilities, mainly represented by baroclinic instabilities, as the Charney type. The latter trigger the subduction of surface winter waters below the ML, injecting in the ocean interior a mode waters core (i.e., the ARMWs), that remains thereafter isolated from the ML and the atmosphere. Agulhas rings with such ARMW core become subsurface-intensified ACes, marked by a layer of low dN^2/dz (and thus low PV). As the submesoscale frontogenesis is not resolved in LR, we observe the development of ARMW only at HR.

5. Intermediate Depths Dynamics

5.1. Mesoscale Stirring of AAIWs

Here we focus on the dynamics at intermediate depths, which in our study region are occupied by AAIWs. Previous numerical and observational studies (Boebel et al., 2003; Rimaud et al., 2012; Rusciano et al., 2012; Schouten et al., 2000) have hypothesized that the regional AAIW dynamics and properties are governed by lateral mesoscale stirring giving rise to strong density-compensated submesoscale thermohaline fronts few kilometers wide. In the 27.2 isopycnal distribution of T, S spiciness and RV, extracted for the same model time step at LR and HR (Figures 9a–9d and 9e–9h, respectively), it is evident that both resolutions exhibit such sharp fronts. This is particularly true for HR, where their distributions show intense fine-scale structures and filaments. The 27.2 isopycnal represents the regional core of AAIW as observed by in situ data (Talley, 1996) and in our simulations (Figure 4 for the HR). Indeed, in the Theta-S diagrams of Figure 9 ("i" for HR and "l" for LR, correspondent to the Theta-S distributions of Figures 9a–9d and 9e–9h), the Theta-S variability is almost completely compensated in its effect on sigma, as highlighted by the noticeable spreading of the Theta-S values concentrated along the 27.2 σ_{theta}.

The contrast in the spatial variability of spiciness between HR and LR (Figures 9d and 9h) show how the two resolutions reproduce different mechanisms of lateral mixing, as further highlighted in section 5.2. This difference is confirmed in the vertical profiles of stratification and spiceness for the two resolutions and seasons (Figure 10): both resolutions are characterized by a positive anomaly of spiciness in the upper layers and negative at depth, but the LR curves of standard deviation are not as tight and close to the mean within the AAIW layer (between 27.2 and 27.6 σ_{theta}) as in the HR. This confirms that the LR does not fully capture the separation between the surface and subsurface dynamical regimes. Moreover, the strongest stratification anomalies, approximately located along the 25.7 and the 26.5 σ_{theta} in summer (Figure 10a) and along the 26.4 and the 27.4 isopycnals in winter (Figure 10c), are always shallower in LR than in HR. This is particularly true in winter, probably due to the large difference in the value of the MLD at this season, between the two model resolutions. This difference has an impact also on the depth of the density-compensated layer: they are always observed at much shallower levels in LR compared to HR (with a vertical difference of about 100 m).

Two main mechanisms have been proposed in the literature to explain the generation of thermohaline structures with weak density signature in the ocean interior: double diffusive instabilities (or lateral intrusions via thermohaline front instabilities), and lateral stirring by mesoscale vortices. It must be first recalled that the

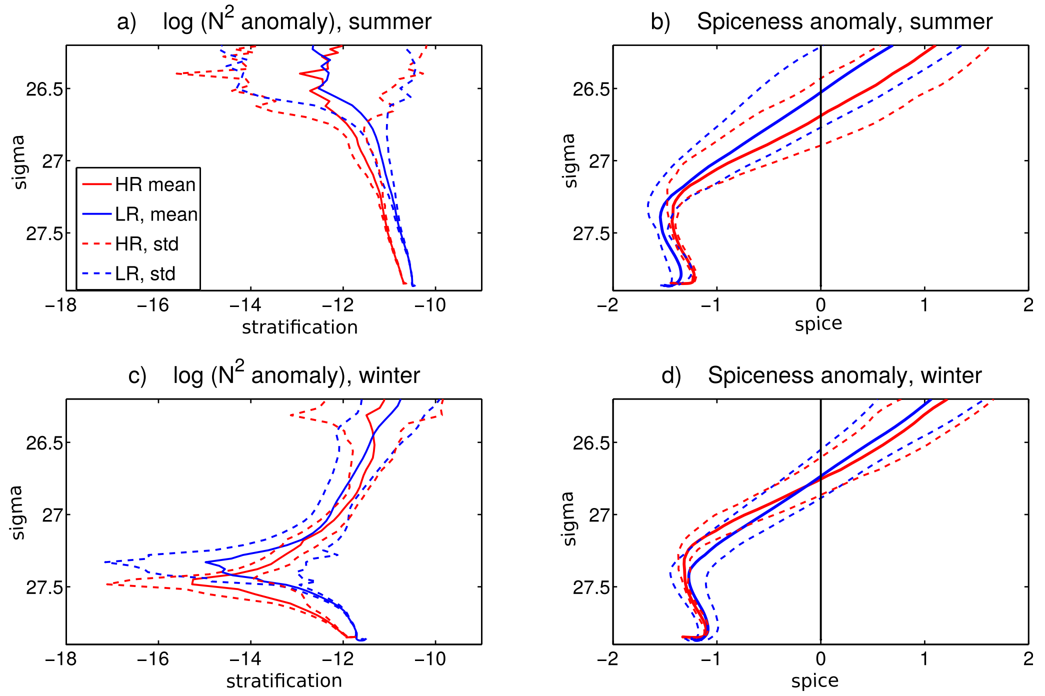

Figure 10. Vertical profiles of the anomaly of stratification (N^2, [s^{-2}]) and spice, against potential density anomaly σ_{theta}, extracted in (top) summer and (bottom) winter for the HR simulation (in red) and the LR solution (in blue). Continuous lines are for the mean values and dashed lines are for the standard deviation.

former can occur in dynamically quiet regions (e.g., for drifting Meddies in the open ocean; Ruddick et al., 2010), whereas the latter always requires a substantial degree of mesoscale turbulence. In our simulations, we did not prescribe different heat and salt diffusivities in the model, thus precluding double diffusion processes. In addition, our study region being a very energetic spot, due to the coexistence of baroclinic eddies with intense lateral gradients of temperature and salinity, the second process is favored (see Klein et al., 1998); this was also found true for AAIW in the Antarctic Circumpolar Current, by Craneguy (1999). Note that though double diffusion may impact filamentogenesis, it is not a necessary condition for its onset as well as for the vertical cascade of tracer variance to occur (see also Meunier et al., 2015). The contrasted structure of spice, showing intense filaments along the 27.2 isopycnal (Figures 9d and 9h) while density is homogeneous (Figures 9i and 9l), indicates that stirring has likely triggered filamentogenesis here.

In terms of orders of magnitude, microstructure intrusions cause lateral fluxes of salt and heat that are often comparable to those by more dynamic, larger scale processes, such as mesoscale eddy stirring or barotropic/baroclinic instability (Ruddick & Richards, 2003). In several locations, like for example within Mediterranean salt lenses, they have been associated to eddy diffusivities of O(3–6 $\times$ 10^3 m^2 s^{-1}) (Ruddick, 1992, 2003). Measurements of isopycnal dispersion due to mesoscale stirring, reported in Ferrari and Polzin (2005), indicate rates somewhat smaller than 1 $\times$ 10^3 m^2 s^{-1}. Hybrid cases, where lateral fluxes can lead to the decay of rings and Meddies, have also been observed. Garrett (1983) showed how fronts can be sharpened by eddy stirring and smoothed by intrusions. In HR, the mean value of horizontal diffusivity along the 27.2 isopycnal is about 3.3 $\times$ 10^3 m^2 s^{-1}, indicating that our study region could also represent a hybrid case. But since the vertical resolution of our nested solution is, at intermediate depths, about 45 m, we are currently not able to resolve the scales of intrusions typical of diapycnal mixing, so we have restricted our analysis to the isopycnal stirring mechanism.

Figure 11a shows a zonal section of *S* for HR in correspondence of a summer ACe. Between the 27.1 and 27.4 isopycnals, interleaving filaments of low *S* appear and have a vertical extension of about 200–300 m, comparable to the observations of Ledwell et al. (1998), and are thus much steeper than the background isopycnals. Their slope is consistent with the *f/N* ratio calculated for submesoscale turbulence and the isotropic forward cascade of tracer variance (Smith & Ferrari, 2009). These low

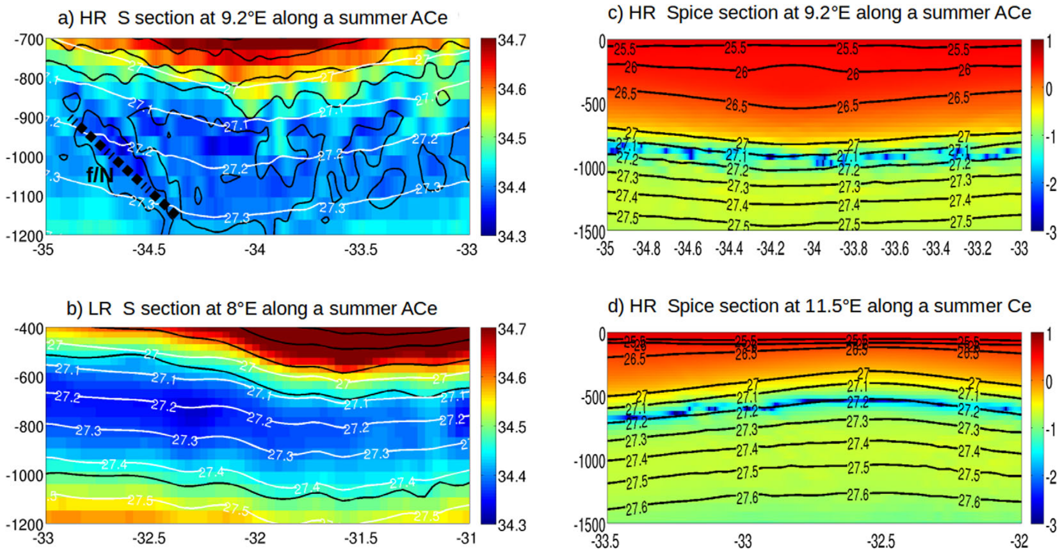

Figure 11. (left) Meridional sections of salinity (psu) plotted at intermediate depths along a summer ACe detected (a) in the HR and (b) in the LR. Color and black contours are for salinity values, while white contours are for isopycnals ranging from 26 to 28 σ_{theta}. In Figure 11a, the *f/N* slope of the tracer filaments is marked by a black, dashed line. (right) Meridional sections of spiciness plotted in summer along (c) an ACe at 9.2°E and (d) a Ce at 11.5°E detected in the HR. Black contours are for isopycnals (26–28 σ_{theta}).

salinities can also be observed at intermediate depths in the LR section (Figure 11b) but here they tend to form uniform layers instead of filaments as in HR. Indeed, only HR is characterized by a layer of negative spiciness below the 27.0 isopycnal, as shown in summer sections below eddies of both polarities (Figures 11c and 11d).

The spiciness is particularly negative along the 27.2 isopycnal. This spiciness minimum layer appears no matter the sign of the eddy and seems to spread across the entire section. The submesoscale, density-compensated thermohaline fronts, arising from the lateral eddy stirring, contribute at these intermediate depths to the vigorous generation of spiceness (Figure 9d) and increased tracer variance in the AAIW layer as shown by the Theta-S diagram of Figure 12. Here the HR Theta-S dispersion (red curves) is high within the AAIW layer, and weak above and below it, in relation with large isopycnal gradients of *T* and *S*. On the contrary, the dispersion is uniform over depth for LR (blue curves in Figure 12). We thus conclude that lateral stirring of tracers by eddies of both signs, in HR, is effective and leads to density-compensated *T* and *S* submesoscale filaments within the AAIWs layer of the Cape Basin. These filaments have scales that cannot be resolved by LR.

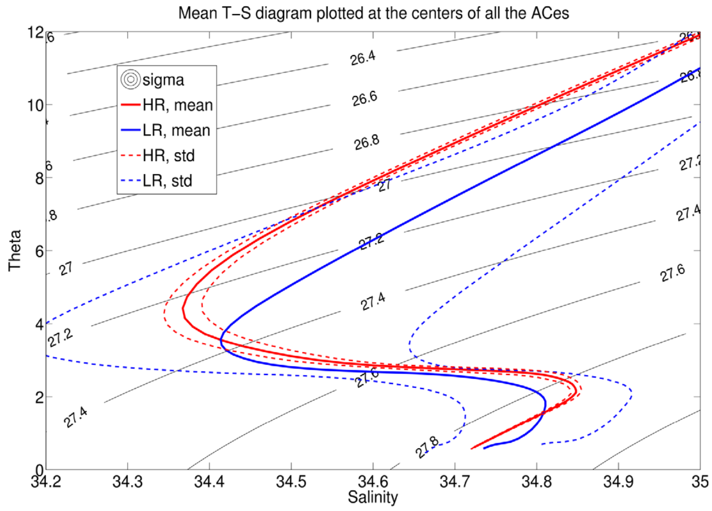

Figure 12. Theta-S diagram showing mean (continuous lines) and standard deviation (dashed) values extracted at AAIW depths at the centers of all the ACes detected in the HR (in red) and in the LR (in blue).

5.2. Which Instabilities at Depth?

In an attempt to investigate the types of instabilities involved in the mechanisms of mesoscale lateral stirring at intermediate depths, we looked at power spectra density (PSD) curves of density, spice (equation (8)), frontogenetic tendency (equation (7)), shear and strain (equation (4)), computed at the isopycnal surface 27.2 for the two model resolutions (Figure 13) during the summer season. Here besides the expected result that LR curves (dashed lines in Figure 13) are flatter and do not reproduce the smaller scales as does HR (continuous lines in the same figure), we observe for HR two peaks: one at $k = 3 \times 10^{-4}$ m^{-1} ($\sim$3 km), which corresponds to the limit between the mesoscale and the submesoscale; and a second peak at $k = 5 \times 10^{-5}$ m^{-1} ($\sim$20 km), that coincides with the mesoscales. These peaks are well marked not only for spice but also for shear

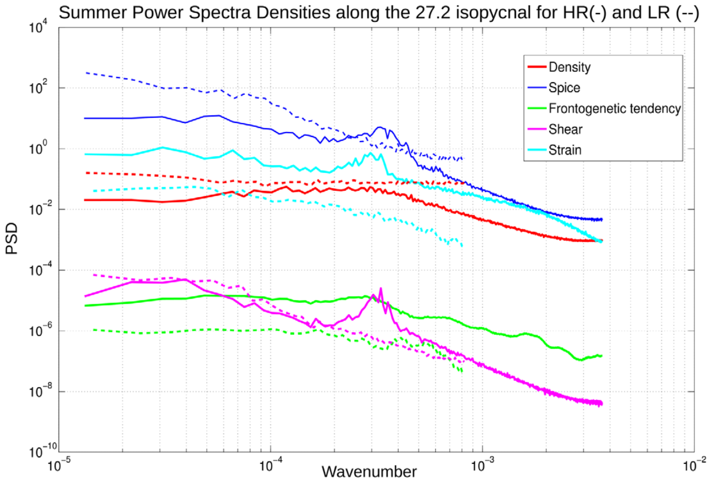

Figure 13. Power spectra densities curves of density, spice, frontogenetic tendency, shear, and strain computed in summer along the 27.2 isopycnal for the HR (continuous lines) and the LR (dashed lines).

and strain. The latter represent the gradients of the velocity field, thus these peaks should be expected also in the PSD of RV.

On the other hand, the density field is smoother; as a consequence, the frontogenetic tendency, which combines the velocity and density gradients, shows a more attenuated peak at the meso/submesoscale transition. At these scales, filamentary and frontal structures are formed in spice and not in density, and are well visible in the HR distributions of shear and strain extracted for summer, at the same time step, along the 27.2 isopycnal (Figures 14a and 14b). Both of them display a clear interweaving of mesoscales and submesoscales, with submesoscale filaments overlaying the eddies; this is particular true for strain (Figure 14b).

Here the sign of its magnitude is positive if the eddy stretches along the *x* axis, as for the Ce centered at 11.5°E–32.5°S, and negative when the eddy is more deformed along the *y* axis, like for the large ACe centered at 9.2°E–34°S that we discussed more in detail in this work. For this ACe, the shear (Figure 14a) shows alternating sign along its largest, meridional axis, mainly driven by the distribution of the "d*U*/d*y*" component (not shown here). Thus, a clear dipolar structure, as the one visible for the eddies centered at 6°E–32.5°S and at 11.5°E–32.5°S, cannot be identified for this ACe, characterized by a highly turbulent pattern of interior shear, driven by very fine scales and possibly by internal gravity waves.

This hypothesis is supported by a vertical section of the horizontal divergence of velocity, plotted along the same ACe (Figure 14c), where alternating, positive and negative, values propagate between the 27 and 27.5 isopycnals. If we reconnect these internal waves and the fine-scale, shear structures to the abundant

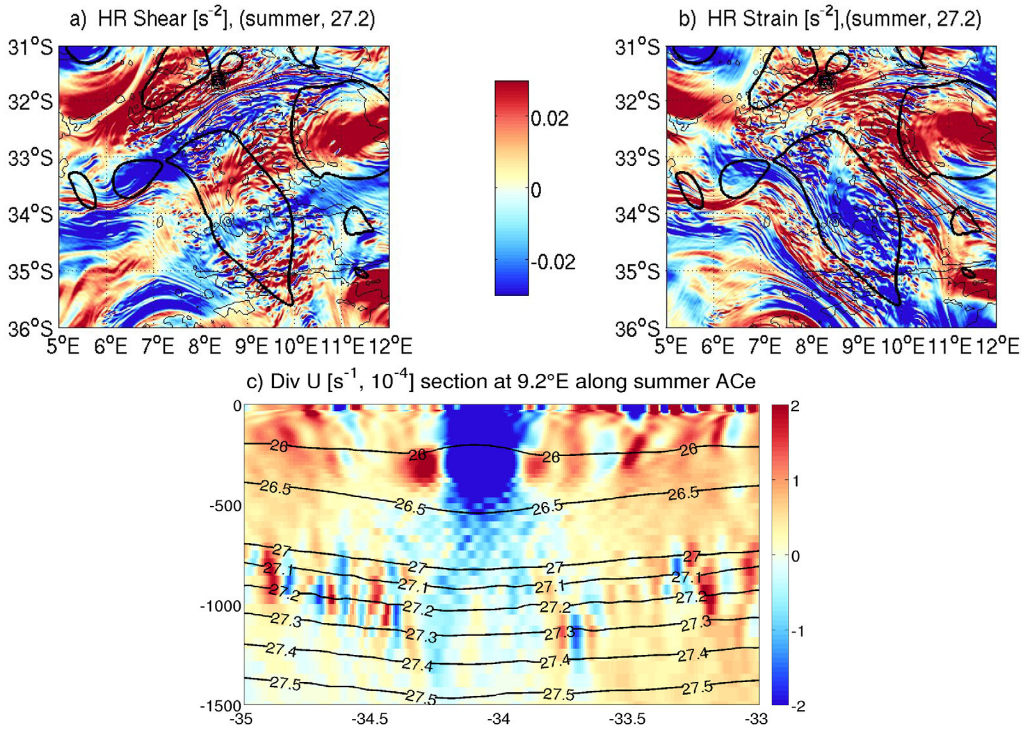

Figure 14. Summer snapshots of (a) shear and (b) strain extracted at $\sigma_{theta} = 27.2$ in the HR. Black contours define the outer limits of the detected eddies. (c) Meridional section of the horizontal divergence of velocity, plotted along a summer ACe of the HR with black contours for isopycnals ranging from 26 to 28 σ_{theta}.

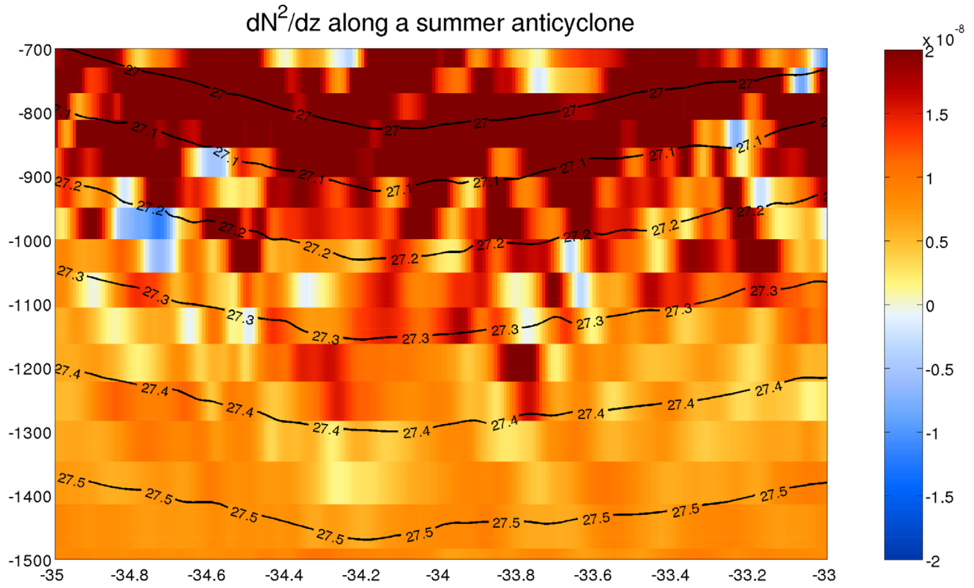

Figure 15. Meridional section of the vertical gradient of stratification (dN^2/dz [s^{-1}]) plotted at 9.2°E along a summer anticyclone for the intermediate depths of the water column (~700–1,500 m). Black contours are for isopycnals ranging from 27 to 27.5 σ_{theta}.

presence of small features and filaments seen in the HR RV snapshot of Figure 10c, different instabilities (C-BCIs, shear or frontal) may be responsible of this turbulent distribution.

To verify if the C-BCI could take place also at greater depths than the base of the ML, and in particular within the AAIW layers, we look at the meridional section of dN^2/dz along the same anticyclone analyzed up to now. In Figure 15, we observe that filaments of negative values of this metric can be actually identified within the 27 and 27.3 isopycnals and therefore these layers could be conducive to this kind of baroclinic instability. However the generation of these filaments could also be related to other unstable mechanisms, like a barotropic instability, their own coiling within the eddy core, after interaction with a neighboring structure, or fine-scale shear and strain. In the latter case, the ratio of vertical shear to horizontal strain would be proportional to N/f (Charney, 1971) and the tracer filaments slope would be much steeper than the typical isopycnal slopes, as seen in our S sections of Figure 11a. We then suggest that C-BCI could develop in the Cape Basin AAIW layer, even though further ad hoc diagnostics would be required to confirm this preliminary evidence.

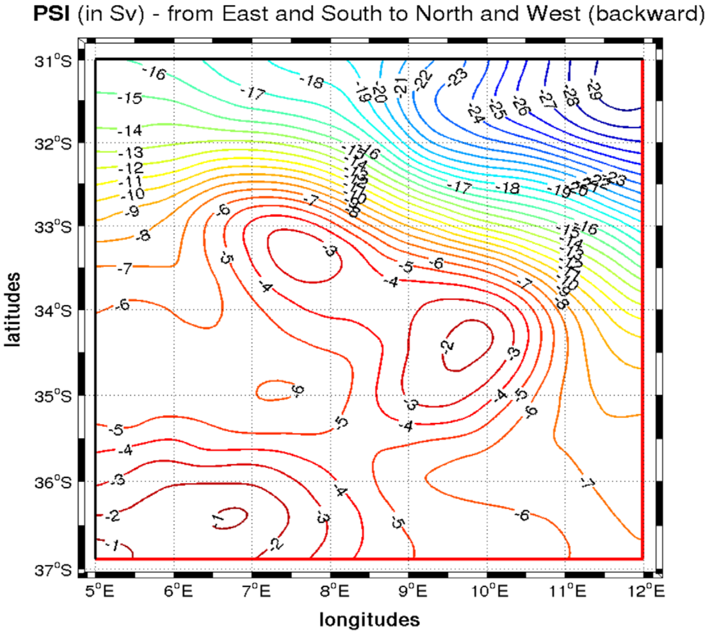

Figure 16. Lagrangian transport stream function estimated within the domain of the second child of the HR (Nested-child2) simulation, with the initial sections colored in red and the final sections in black.

6. Impact of Smaller Scales on the Indo-Atlantic Exchange

In this section, we use a Lagrangian approach to quantify the impact of smaller-scales dynamics in the Indo-Atlantic transport of thermocline water masses. Integration of particles trajectories were performed for the two simulations analyzed in this work (HR and LR) using the offline mass-preserving algorithm ARIANE (Blanke et al., 1999; Blanke & Raynaud, 1997) applied to daily archives of the multiyear, three-dimensional velocity field. This methodology allows the full description of individual trajectories as well as volume transport estimates based on the tiny weight allotted to each particle and transported without alteration along its trajectory. The volume of water transported from an initial to a final geographical

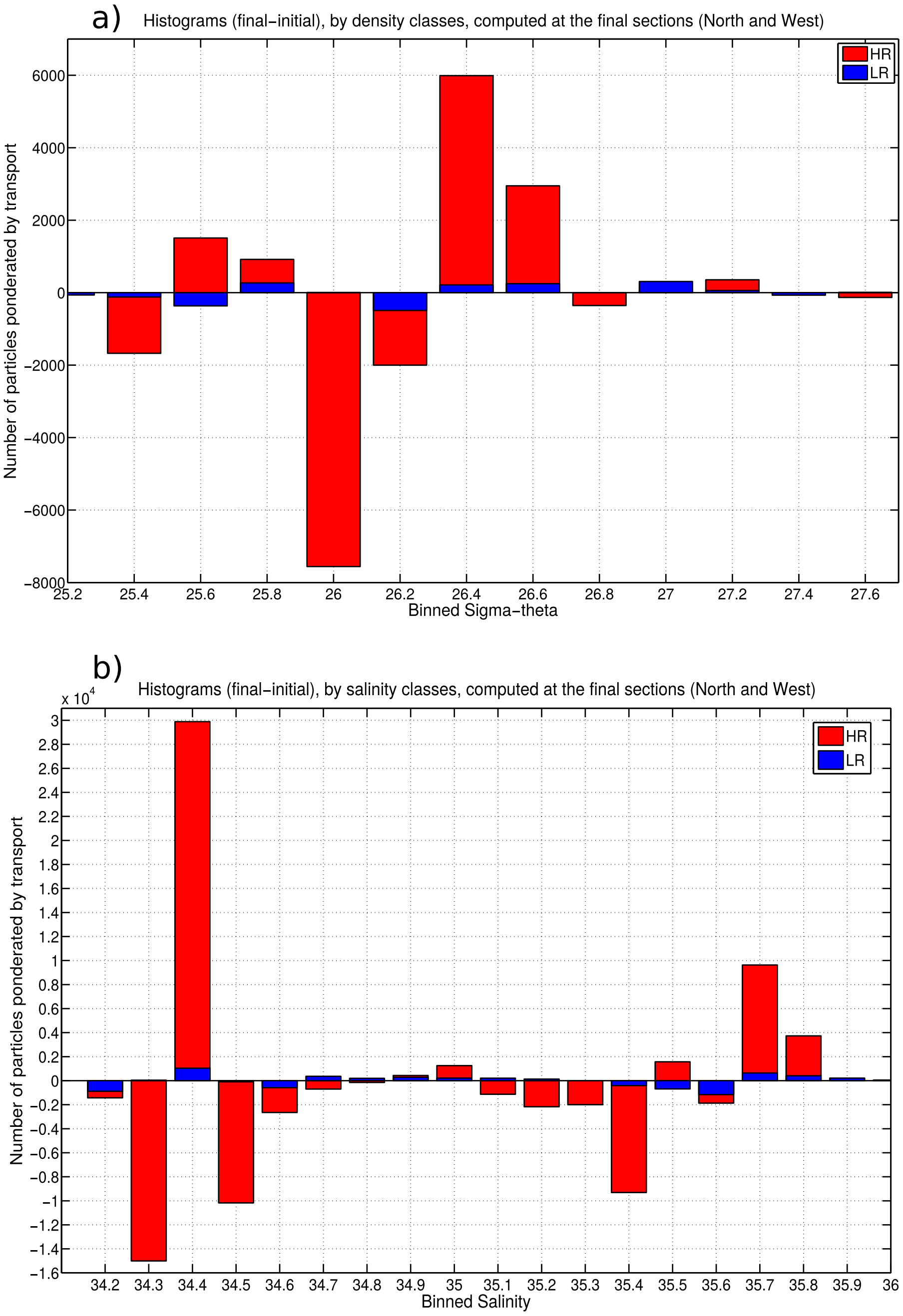

Figure 17. Histograms of the differences between the final and initial Lagrangian transports (Sv), binned by (a) potential density anomaly (σ_{theta}) and (b) salinity classes, for the HR (in red) and for the LR (in blue) simulations.

section is computed by summing the transport of the particles achieving the connection that is being considered. Default information interpolated along individual trajectories includes salinity, temperature, depth, and density.

Our Lagrangian experiments were conducted over the control domain corresponding to the geographical extension of the HR solution, as shown in the transport stream function map of Figure 16. The particles were initialized at the initial sections located at the eastern and southern boundaries and intercepted at the western and northern boundaries of this control domain (respectively traced in red and black in Figure 16). Over these geographical sections where millions of particles were spread (to account for an inward velocity), we kept only the particles associated with relevant salinity and density values typical of thermocline waters in the Cape Basin, meaning using their values from the surface to the 27.6 isopycnal. Each particle was associated with an individual weight related to the local magnitude of the incoming transport (expressed here in sverdrups, with 1 Sv $= 10^6$ m^3 s^{-1}). All particles were integrated backward in time and the starting dates were sequentially taken during the last 4 years of the available archive, giving a total transport of about 30 Sv for HR (Figure 16) and of $\sim$20 Sv for LR. We then plotted histogram bars of the difference between the final and the initial transports, computed as the number of particles normalized by their total transport and binned by potential density classes (Figure 17a). We verified that the highest resolutions simulation (in red in Figure 17a) is the only one able to capture a prominent, net transport, from the Indian to the Atlantic oceans, of thermocline waters, mainly consisting of the lighter (isopycnal layers 25.6–25.8) and denser (isopycnal layers 26.4–26.6) varieties of mode water, and to a lesser extent of intermediate waters (isopycnal layers 27.2). If we plot the same Lagrangian estimates binned by salinity classes (Figure 17b), we observe for intermediate waters a net transport in correspondence of the IA-AAIW salinity class ($S = 34.4$ psu), which results from the lateral mixing of the Indian and Atlantic AAIWs. Both of these figures show that small-scale dynamics strongly influence mode and intermediate water properties by efficiently forming and transforming water masses. These "in route" transformations affect the water properties of the Indo-Atlantic transport, acting on the interocean fluxes of heat and freshwater and therefore on the AMOC.

7. Summary and Conclusions

The Indo-Atlantic exchange of thermocline and intermediate waters is essential in maintaining the AMOC, by providing the return flow to the North Atlantic and compensating the North Atlantic Deep Water outflow to the Southern Ocean (Gordon et al., 1992; Speich et al., 2007). This mainly happens through Agulhas rings injected into the Cape Basin, in the southeasternmost corner of the Atlantic, after detachment from the AC at the AR, thus representing the major cause of current variability in this region (Garzoli et al., 1996).

Several issues are important to assess more accurately how Agulhas rings contribute to interocean fluxes (Lutjeharms et al., 2003). These naturally include their horizontal and vertical dimensions, as well as their anomalous heat and salt contents soon after having been spawned (Schmid et al., 2003). In this paper, we analyzed some of these aspects, investigating the geometry of the simulated ACes and their thermohaline structure, as well as the impact that these turbulent features have on the local water masses properties and advection. We have also pointed out that different types of instabilities develop within these rings during their journey in the Cape Basin, where they interact among themselves and with eddies of opposite sign.

Previous numerical studies (Matano & Beier, 2003; Weijer et al., 2013; Wells et al., 2000) have shown that both barotropic and baroclinic processes play a major role as triggering mechanisms of eddies generation in the greater Agulhas Current System. In our work, we have further investigated the relative importance of these two main mechanisms of eddies interactions within the Cape Basin, underlining their role in producing finer scales turbulence. We used two regional numerical simulations, run respectively at mesoscale and submesoscale-resolving resolutions. We first discriminated the range of scales and turbulent processes that each of these simulations is able to resolve. Then, by the analysis of specific diagnostics, applied to the eddies detected within our study region, we have quantified the energy contents and transfers at different scales and assessed their effects on the formation and transformation of the local water masses. The results were here discussed for a summer and a winter ACes, chosen, in each of the two simulations, to represent the mean behavior of the simulated Agulhas rings.

Our main finding consisted in demonstrating a clear vertical separation between the dynamical regimes prevailing in the upper and intermediate depth layers. At the surface and down to the base of the ML, enhanced values of EKE, VBF and frontogenesis are related to the seasonal development of different instabilities: MLIs, symmetric and C-BCIs. MLIs mainly dominate in winter, when the action of the atmospheric forcing is more important and leads to a significant deepening of the ML. Because these instabilities are at a submesoscale exclusively solved by HR, only this simulation captured a correct seasonal cycle of the MLD. The same result holds for symmetric and shear instabilities, triggered by the interaction of mesoscale barotropic instabilities and mainly active, in our study region, during summer, when small meanders and filaments appear around and within mesoscale eddies.

We have also shown that these two seasonal, dynamical regimes are involved, via C-BCIs, in the formation of a local variety of mode waters, ARMW, commonly found in the core of Agulhas rings. C-BCIs are triggered in winter, engendering the subduction of surface waters below the ML where they form thick homogeneous layers of mode waters. Below the thermocline, frontal instabilities seem to develop, at both seasons, due to the interaction between adjacent eddies of opposite signs, leading to deformations of the eddy geometry and likely affecting its 3-D structure and thermohaline content.

For intermediate depths, we have provided evidence of relevant mechanisms of density compensation and lateral stirring of thermohaline fronts, driven by the intense mesoscale and submesoscale fields. In fact, similarly to the intrusions of the Mediterranean Water Overflow into the intermediate layers of the North Atlantic (Smith & Ferrari, 2009), a vigorous geostrophic eddy field, developed through baroclinic instability of the mean flow, has been documented in the literature within the Cape Basin (Boebel et al., 2003; Matano & Beier, 2003; Treguier et al., 2003). Here the mesoscale eddies stretch and twist the intense T-S gradients and produce sharp submesoscale T-S filaments along isopycnals. The eddy generation of submesoscale T-S variance is particularly effective at the depth of AAIWs, where salty and warm Indian AAIW converges and mixes with the fresher and colder Atlantic AAIW variety (Rimaud et al., 2012; Rusciano et al., 2012). Therefore, our work endorses the assumption of Smith and Ferrari (2009) that in regions characterized by large water mass contrasts, the generation of compensated submesoscale T-S gradients by lateral mesoscale eddy stirring can overcome the generation of T-S variance by vertical turbulence. This hypothesis could be further investigated through the adoption of a more idealized, numerical approach. Here by taking a S-QG approach, we only explored the possibility that C-BCIs can dynamically couple layers within the ocean interior characterized by marked changes in stratification.

By using Lagrangian diagnostics, we finally showed the impact of resolving smaller-scale processes assumes on the simulated Indo-Atlantic exchange of subsurface water masses. These transports estimates indicate that only at HR the model can depict the interocean transfer of upper and lower thermocline waters, by capturing the formation and advection of different types of mode waters (ARMW) and the AAIW transformation in its regional varieties. Although more experimental studies are needed to corroborate the generality of the present results, we conclude by reiterating the key role of mesoscale and submesoscale processes in driving and structuring the advection of subsurface water masses in the Cape Basin. These water masses materialize the Indo-Atlantic exchange, and thus rule the related heat and salt anomalies penetrating into the Atlantic Ocean and ultimately influencing the AMOC. The two configurations, run at different horizontal resolutions in our study, highlight that, in order to correctly represent the observed transport and water masses properties involved in this exchange, the simulated scales need to include a large portion of the submesoscale spectrum.

Acknowledgments
The model data used analyzed in this paper are available at the following website: http://data.umr-lops.fr/pub/AGU_LH_HR/. The authors greatly appreciate discussions with Xavier Capet, Gildas Cambon, Guillaume Lapeyre, Guillaume Roullet, Bernard Barnier, Arne Biastoch, and Jeroen Molemaker. This work was supported by the "Laboratoire d'Excellence" LabexMER (ANR-10-LABX-19), by a grant from the French Government under the program "Investissements d'Avenir," and by a grant from the Regional Council of Brittany. This work was also supported by the European Union Horizon 2020 research and innovation programme under grant 633211 (AtlantOS), and by the 11-ANR-56-004 SAMOC research grant. This study is part of the CLIVAR-SAMOC international initiative. We also acknowledge funding from the ANR/DGA program DYNED ATLAS and the French CNRS computer center IDRIS for technical and computational support. We thank both reviewers who helped us to improve this manuscript.

References

Arhan, M., Mercier, H., & Lutjeharms, J. R. E. (1999). The disparate evolution of three Agulhas rings in the South Atlantic Ocean. *Journal of Geophysical Research*, *104*, 20987–21005. https://doi.org/10.1029/1998JC900047

Arhan, M., Speich, S., Messager, C., Dencausse, G., Fine, R., & Boye, M. (2011). Anticyclonic and cyclonic eddies of subtropical origin in the subantarctic zone south of Africa. *Journal of Geophysical Research*, *116*, C11004. https://doi.org/10.1029/2011JC007140

Ayina, H.-L., Bentamy, A., Mestas-Nuez, A. M., & Madec, G. (2006). The impact of satellite winds and latent heat fluxes in a numerical simulation of the tropical Pacific Ocean. *Journal of Climate*, *19*, 5889–5902. https://doi.org/10.1175/JCLI3939.1

Beal, L. M., de Ruijter, W. P. M., Biastoch, A., & Zahn, R., & SCOR/IAPSO/WCRP Working Group 136. (2011). On the role of the Agulhas System in Ocean Circulation and Climate. *Nature*, *472*, 429–436. https://doi.org/10.1038/nature09983

Bentamy, A., Katsaros, K. B., Alberto, M., Drennan, W. M., Forde, E. B., & Roquet, H. (2003). Satellite estimates of wind speed and latent heat flux over the global oceans. *Journal of Climate*, *16*, 637–656. https://doi.org/10.1175/1520-0442(2003)016<0637:SEOWSA>2.0.CO;2

Biastoch, A., Boning, C. W., & Lutjeharms, J. R. E. (2008). Agulhas leakage dynamics affects decadal variability in Atlantic overturning circulation. *Nature*, *456*, 489–492. https://doi.org/10.1038/nature07426

Blanke, B., Arhan, M., Madec, G., & Roche, S. (1999). Warm water paths in the Equatorial Atlantic as diagnosed with a general circulation model. *Journal of Physical Oceanography*, *29*, 2753–2768. https://doi.org/10.1175/1520-0485(1999)029<2753:WWPITE>2.0.CO;2

Blanke, B., & Raynaud, S. (1997). Kinematics of the Pacific Equatorial Undercurrent: An Eulerian and Lagrangian approach from GCM results. *Journal of Physical Oceanography*, *27*, 1038–1053. https://doi.org/10.1175/1520-0485(1997)027<1038:KOTPEU>2.0.CO;2

Boccaletti, G., Ferrari, R., & Fox-Kemper, B. (2007). Mixed layer instabilities and restratification. *Journal of Physical Oceanography*, *37*(9), 2228–2250. https://doi.org/10.1175/JPO3101.1

Boebel, O., Duncombe Rae, C., Garzoli, S., Lutjeharms, J., Richardson, P., Rossby, T., et al. (1998). Float experiment studies interocean exchanges at the tip of Africa. *Eos, Transactions American Geophysical Union*, *79*(1), 6–8.

Boebel, O., Lutjeharms, J. R. E., Schmid, C., Zenk, C., Rossby, T., & Barron, C. (2003). The Cape Cauldron: A regime of turbulent inter-ocean exchange. *Deep Sea Research Part I: Oceanographic Research Papers*, *50*, 57–86. https://doi.org/10.1016/S0967-0645(02)00379-X

Brannigan, L. (2016). Intense submesoscale upwelling in anticyclonic eddies. *Geophysical Research Letters*, *43*, 3360–3369. https://doi.org/10.1002/2016GL067926

Brannigan, L., Marshall, D., Naveira-Garabato, A., & Nurser, G. (2015). The seasonal cycle of submesoscale flows. *Ocean Modelling*, *92*, 69–84.

Bruggemann, N., & Eden, C. (2015). Routes to dissipation under different dynamical conditions. *Journal of Physical Oceanography*, *45*(8), 2149–2168. https://doi.org/10.1175/JPO-D-14-0205.1

Byrne, D. A., Gordon, A. L., & Haxby, W. F. (1995). Agulhas eddies: A synoptic view using Geosat ERM data. *Journal of Physical Oceanography*, *25*, 902–917.

Callies, J., Ferrari, R., Klymak, J. M., & Gula, J. (2015). Seasonality in submesoscale turbulence. *Nature Communications*, *6*, 6862.

Capet, X., McWilliams, J. C., Molemaker, M. J., & Shchepetkin, A. F. (2008a). Mesoscale to submesoscale transition in the California Current System. Part I: Flow structure, eddy flux, and observational tests. *Journal of Physical Oceanography*, *38*, 2943.

Capet, X., McWilliams, J., Molemaker, M., & Shchepetkin, A. (2008b). Mesoscale to submesoscale transition in the California current system. Part III: Energy balance and flux. *Journal of Physical Oceanography*, *38*(10), 2256–2269.

Capet, X., Roullet, G., Klein, P., & Maze, G. (2016). Intensification of upper-ocean submesoscale turbulence through Charney baroclinic instability. *Journal of Physical Oceanography*, *46*, 3365–3384. https://doi.org/10.1175/JPO-D-16-0050.1

Chaigneau, A., Gizolme, A., & Grados, C. (2008). Mesoscale eddies off Peru' in altimeter records: Identification algorithms and eddy spatio-temporal patterns. *Progress in Oceanography*, *79*(2), 106–119.

Charney, J. G. (1947). The dynamics of long waves in a baroclinic westerly current. *Journal of Meteorology*, *4*, 136–162. https://doi.org/10.1175/1520-0469(1947)004<0136:TDOLWI>2.0.CO;2

Charney, J. G. (1971). Geostrophic turbulence. *Journal of the Atmospheric Sciences*, *28*, 1087–1095.

Craneguy, P. (1999). *Mecanismes d'intrusion de l'eau antarctique intermediaire antarctique a travers le courant circumpolaire antarctique* (PhD thesis).

Da Silva, A. M., Young-Molling, C. C., & Levitus, S. (1994). Atlas of surface marine data 1994, vol. 1. Algorithms and procedures. In *NOAA atlas NESDIS* (Vol. 6). Silver Spring, MD: NOAA.

Debreu, L., & Mazauric, C. (2006). *Adaptive Grid Refinement (AGRIF) in Fortran 90: Users guide version 1.3*. Retrieved from http://www-lmc.imag.fr/IDOPT/AGRIF/index.html

Dencausse, G., Arhan, M., & Speich, S. (2010). Spatio temporal characteristics of the Agulhas Current retroflection. *Deep Sea Research Part I: Oceanographic Research Papers*, *57*(11), 1392–1405. https://doi.org/10.1016/j.dsr.2010.07.004

De Ruijter, W. P. M., Biastoch, A., Drijfhout, S. S., Lutjeharms, J. R. E., Matano, R. P., Pichevin, T., et al. (1999). Indian-Atlantic inter-ocean exchange: Dynamics, estimation and impact. *Journal of Geophysical Research*, *104*, 20885–20911.

Drijfhout, S. S., Kattenberg, A., Haarsma, R. J., & Selten, F. M. (2001). The role of the ocean in midlatitude, interannual-to-decadal-timescale climate variability of a coupled model. *Journal of Climate*, *14*(17), 3617–3630. https://doi.org/10.1175/1520-0442(2001)014<3617:TROTOI>2.0.CO;2

Ertel, H. (1942). Ein neuer hydrodynamischer Erhaltungssatz. *Naturwiss*, *30*, 543–544.

Ferrari, R., & Polzin, K. (2005). Finescale structure of the T–S relation in the eastern North Atlantic. *Journal of Physical Oceanography*, *35*, 1437–1454.

Fox-Kemper, B., Ferrari, R., & Hallberg, R. (2008). Parameterization of mixed layer Eddies. Part I: Theory and diagnosis. *Journal of Physical Oceanography*, *38*(6), 1145–1165. https://doi.org/10.1175/2007JPO3792.1

Garrett, C. (1983). On the initial streakiness of a dispersing tracer in two- and three-dimensional turbulence. *Dynamics of Atmospheres and Oceans*, *7*, 265–277.

Garzoli, S. L., & Gordon, A. L. (1996). Origins and variability of the Benguela Current. *Journal of Geophysical Research*, *101*, 897–906.

Garzoli, S. L., Gordon, A. L., Kamenkovich, V., Pillsbury, D., & Duncombe Rae, C. (1996). Variability and sources of the southeastern Atlantic circulation. *Journal of Marine Research*, *54*, 1039–1071.

Giordani, H., & Caniaux, G. (2001). Sensitivity of cyclogenesis to sea surface temperature in the Northwestern Atlantic. *Monthly Weather Review*, *129*(6), 1273–1295.

Giulivi, C. F., & Gordon, A. L. (2006). Isopycnal displacements within the Cape Basin thermocline as revealed by the Hydrographic Data Archive. *Deep Sea Research Part I: Oceanographic Research Papers*, *53*(8), 1285–1300.

Gladyshev, S., Arhan, M., Sokov, A., & Speich, S. (2008). A hydrographic section from South Africa to the southern limit of the Antarctic Circumpolar Current at the Greenwich meridian. *Deep Sea Research Part I: Oceanographic Research Papers*, *55*(10), 1284–1303. https://doi.org/10.1016/j.dsr.2008.05.009

Goni, G. J., Garzoli, S. L., Roubicek, A. J., Olson, D. B., & Brown, O. B. (1997). Agulhas ring dynamics from TOPEX/POSEIDON satellite altimeter data. *Journal of Marine Research*, *55*, 861–883.

Gordon, A. L. (1985). Indian-Atlantic transfer of thermocline water at the Agulhas Retroflection. *Science*, *227*, 1030–1033.

Gordon, A. L., & Haxby, W. F. (1990). Agulhas eddies invade the South Atlantic: Evidence from Geosat altimeter and shipboard CTD survey. *Journal of Geophysical Research*, *95*, 3117–3125.

Gordon, A. L., Weiss, R. F., Smethie, W. M., Jr., & Warner, M. J. (1992). Thermocline and intermediate water communication between the South Atlantic and Indian Oceans. *Journal of Geophysical Research*, *97*, 7223–7240. https://doi.org/10.1029/92JC00485

Gula, J., Molemaker, M. J., & McWilliams, J. C. (2015). Topographic vorticity generation, submesoscale instability and vortex street formation in the Gulf Stream. *Geophysical Research Letters*, *42*, 4054–4062. https://doi.org/10.1002/2015GL063731

Haine, T. W. N., & Marshall, J. (1998). Gravitational, symmetric, and baroclinic instability of the ocean mixed layer. *Journal of Physical Oceanography*, *28*(4), 634–658.

Hogg, N. G., & Stommel, H. M. (1985). The Heton, an elementary interaction between discrete baroclinic geostrophic vortices, and its implications concerning heat-flow. *Proceedings of the Royal Society of London, Series A*, *397*, 1–20.

Hua, B.-L., Ménesguen, C., Le Gentil, S., Schopp, R., Marsset, B., & Aiki, H. (2013). Layering and turbulence surrounding an anticyclonic oceanic vortex: In situ observations and quasi-geostrophic numerical simulations. *Journal of Fluid Mechanics*, *731*, 418–442.

Jacobs, S. S., & Georgi, D. T. (1977). Observations on the southwest Indian/Antarctic Ocean. In M. Angel (Ed.), *A voyage of discovery* (pp. 43–84). Oxford, UK: Pergamon.

Klein, P., Lien Hua, B., Lapeyre, G., Capet, X., LeGentil, S., & Sasaki, H. (2008). Upper ocean turbulence from high-resolution 3D simulations. *Journal of Physical Oceanography*, *38*, 1748–1763.

Klein, P., Treguier, A. M., & Hua, B. L. (1998). Three-dimensional stirring of thermohaline fronts. *Journal of Marine Research*, *56*, 589–612.

Lapeyre, G., Klein, P., & Hua, B. L. (2006). Oceanic restratification forced by surface frontogenesis. *Journal of Physical Oceanography*, *36*(8), 1577–1590.

Large, W. G., McWilliams, J. C., & Doney, S. C. (1994). Oceanic vertical mixing: A review and a model with a nonlocal boundary layer parameterization. *Reviews of Geophysics*, *32*, 363–403.

Laxenaire, R., Speich, S., Blanke, B., Chaigneau, A., & Pegliasco, C. (2018). New insights on Agulhas rings dynamics as inferred from altimetry, in press.

Ledwell, J. R., Watson, A. J., & Law, C. S. (1998). Mixing of a tracer in the pycnocline. *Journal of Geophysical Research*, *103*, 21499–21529.

Lemarie, F., Kurian, J., Shchepetkin, A. F., Molemaker, M. J., Colas, F., & McWilliams, J. C. (2012). Are there inescapable issues prohibiting the use of terrain-following coordinates in climate models? *Ocean Modelling*, *42*, 57–79. https://doi.org/10.1016/j.ocemod.2011.11.007

Lutjeharms, J. R. E. (1996). The exchange of water between the south Indian and south Atlantic oceans. In G. Wefer (Ed.), *The South Atlantic: Present and past circulation* (pp. 125–162). New York, NY: Springer.

Lutjeharms, J. R. E., de Ruijter, W. P. M., & Peterson, R. G. (1992). Inter-basin exchange and the Agulhas Retroflection; the development of some oceanographic concepts. *Deep Sea Research Part A. Oceanographic Research Papers*, *39*, 1791–1807.

Lutjeharms, J. R. E., & Gordon, A. L. (1987). Shedding of an Agulhas Ring observed at sea. *Nature*, *325*, 138–140.

Lutjeharms, J. R. E., Penven, P., & Roy, C. (2003). Modelling the shear-edge eddies of the southern Agulhas Current. *Continental Shelf Research*, *23*, 1099–1115.

Marchesiello, P., McWilliams, J. C., & Shchepetkin, A. F. (2001). Open boundary conditions for long-term integration of regional oceanic models. *Ocean Modelling*, *3*, 1–20. https://doi.org/10.1016/S1463-5003(00)00013-5

Matano, R., & Beier, E. J. (2003). A kinematic analysis of the Indian/Atlantic interocean exchange. *Deep Sea Research Part II: Topical Studies in Oceanography*, *50*, 229–249. https://doi.org/10.1016/S0967-0645(02)00395-8

Mensa, J. A., Garraffo, Z., Griffa, A., Ozgokmen, T. M., Haza, A., & Veneziani, M. (2013). Seasonality of the submesoscale dynamics in the Gulf stream region. *Ocean Dynamics*, *63*(8), 923–941. https://doi.org/10.1007/s10236-013-0633-1

McDonagh, E. L., Heywood, K. J., & Meredith, M. P. (1999). On the structure, paths, and fluxes associated with Agulhas rings. *Journal of Geophysical Research*, *104*, 21007–21020. https://doi.org/10.1029/1998JC900131

McWilliams, J. C. (2008). The nature and consequences of oceanic eddies. In M. Hecht and H. Hasumi (Eds.), *Eddy-resolving ocean modeling, AGU monograph* (pp. 5–15). Washington, DC: AGU.

McWilliams, J. C., & Molemaker, M. J. (2011). Baroclinic frontal arrest: A sequel to unstable frontogenesis. *Journal of Physical Oceanography*, *41*(3), 601–619. https://doi.org/10.1175/2010JPO4493.1

Meunier, T., Mnesguen, C., Schopp, R., & Le Gentil, S. (2015). Tracer stirring around a Meddy: The formation of layering. *Journal of Physical Oceanography*, *45*, 407–423.

Molemaker, M. J., McWilliams, J. C., & Capet, X. (2010). Balanced and unbalanced routes to dissipation in an equilibrated Eady flow. *Journal of Fluid Mechanics*, *654*, 35–63. https://doi.org/10.1017/S0022112009993272

Okubo, A. (1970). Horizontal dispersion of floatable particles in the vicinity of velocity singularities such as convergences. *Deep Sea Research and Oceanographic Abstracts*, *17*, 445–454.

Ou, H. W., & de Ruijter, W. P. M. (1986). Separation of an inertial boundary current from a curved coastline. *Journal of Physical Oceanography*, *26*, 2267–2279.

Peliz, A., Boutov, D., Aguiar, A. B., & Carton, X. (2014). The Gulf of Cadiz Gap wind anticyclones. *Continental Shelf Research*, *91*, 171–191.

Penven, P., Chang, N., & Shillington, F. (2006). Modelling the Agulhas Current using SAfE (Southern African experiment). *Geophysical Research Abstracts*, *8*(04225).

Reason, C. J. C. (2001). Evidence for the influence of the Agulhas Current on regional atmospheric circulation patterns. *Journal of Climate*, *14*, 2769–2778.

Rimaud, J., Speich, S., Blanke, B., & Nicolas, N. (2012). The exchange of Intermediate Water in the southeast Atlantic: Water mass transformations diagnosed from the Lagrangian analysis of a regional ocean model. *Journal of Geophysical Research*, *117*, C08034. https://doi.org/10.1029/2012JC008059

Rubio, A., Blanke, B., Speich, S., Grima, N., & Roy, C. (2009). Mesoscale eddy activity in the southern Benguela upwelling system from satellite altimetry and model data. *Progress in Oceanography*, *83*, 288–295. https://doi.org/10.1016/j.pocean.2009.07.029

Ruddick, B., & Richards, K. (2003). Oceanic thermohaline intrusions: Observations. *Progress in Oceanography*, *56*(3–4), 499–527.

Ruddick, B. R. (1992). Intrusive mixing in a Mediterranean salt lens intrusion slopes and dynamical mechanisms. *Journal of Physical Oceanography*, *22*, 1274–1285.

Ruddick, B. R. (2003). Sounding out fine structures. *Science*, *301*(5634), 772–773. https://doi.org/10.1126/science.1086924

Ruddick, B. R., Oakey, N. S., & Hebert, D. (2010). Measuring lateral heat flux across a thermohaline front: A model and observational test. *Journal of Marine Research*, *68*(3–4), 523–539.

Rusciano, E., Speich, S., & Ollitrault, M. (2012). Interocean exchanges and the spreading of Antarctic Intermediate Water south of Africa. *Journal of Geophysical Research*, *117*, C10010. https://doi.org/10.1029/2012JC008266

Schmid, C., Boebel, O., Zenk, W., Lutjeharms, J. R. E., Garzoli, S. L., Richardson, P. L., et al. (2003). Early evolution of an Agulhas Ring. *Deep Sea Research Part II: Topical Studies in Oceanography*, *50*(1), 141–166.

Schouten, M. W., de Ruijter, W. P. M., van Leeuwen, P. J., & Lutjeharms, J. R. E. (2000). Translation, decay and splitting of Agulhas rings in the south-eastern Atlantic ocean. *Journal of Geophysical Research*, *105*, 21913–21925.

Shchepetkin, A. F., & McWilliams, J. C. (2003). A method for computing horizontal pressure-gradient force in an oceanic model with a nonaligned vertical coordinate. *Journal of Geophysical Research*, *108*(C3), 3090. https://doi.org/10.1029/2001JC001047

Shchepetkin, A. F., & McWilliams, J. C. (2005). The regional oceanic modeling system (ROMS): A split-explicit, free-surface, topography-following-coordinate oceanic model. *Ocean Modelling*, *9*, 304–347. https://doi.org/10.1016/j.ocemod.2004.08.002

Shchepetkin, A. F., & McWilliams, J. C. (2009). Correction and commentary for ocean forecasting in terrain-following coordinates: Formulation and skill assessment of the regional ocean modeling system by Haidvogel et al. *Journal of Computational Physics*, *227*, 3595–3624.

Smith, K. S., & Ferrari, R. (2009). The production and dissipation of compensated thermohaline variance by mesoscale stirring. *Journal of Physical Oceanography*, *39*, 2477–2501. https://doi.org/10.1175/2009JPO4103.1

Smith, W., & Sandwell, D. (1997). Global sea floor topography from satellite altimetry and ship depth soundings. *Science*, *277*(5334), 1956–1962. https://doi.org/10.1126/science.277.5334.1956

Spall, M. A. (1995). Frontogenesis, subduction, and cross-front exchange at upper ocean fronts. *Journal of Geophysical Research*, *100*, 2543–2557. https://doi.org/10.1029/94JC02860

Speich, S., & Arhan, M. (2007). GOODHOPE/Southern Ocean: A study and monitoring of the Indo-Atlantic connections. *Mercator Newsletter*, *27*, 2941.

Speich, S., Blanke, B., & Cai, W. (2007). Atlantic Meridional Overturning and the Southern Hemisphere Supergyre. *Geophysical Research Letters*, *34*, L23614. https://doi.org/10.1029/2007GL031583

Speich, S., Lutjeharms, J. R. E., Penven, P., & Blanke, B. (2006). Role of bathymetry in Agulhas Current configuration and behaviour. *Geophysical Research Letters*, *33*, L23611. https://doi.org/10.1029/2006GL027157

Talley, L. D. (1996). Antarctic Intermediate Water in the South Atlantic. In G. Wefer (Ed.), *The South Atlantic: Present and past circulation* (pp. 219–238). Berlin, Germany: Springer. https://doi.org/10.1007/978-3-642-80353-6-11

Thomas, L. N. (2005). Destruction of potential vorticity by winds. *Journal of Physical Oceanography*, *35*(12), 2457–2466.

Thomas, L. N., Taylor, J. R., D'Asaro, E. A., Lee, C. M., Klymak, J. M., & Shcherbina, A. (2016). Symmetric instability, inertial oscillations, and turbulence at the Gulf Stream Front. *Journal of Physical Oceanography*, *46*, 197–217. https://doi.org/10.1175/JPO-D-15-0008.1

Thomas, L. N., Taylor, J. R., Ferrari, R., & Joyce, T. M. (2013). Symmetric instability in the Gulf Stream. *Deep Sea Research Part II: Topical Studies in Oceanography*, *91*, 96–110. https://doi.org/10.1016/j.dsr2.2013.02.025

Treguier, A.-M., Boebel, O., Barnier, B., & Madec, G. (2003). Agulhas eddy fluxes in a 1/6° Atlantic model. *Deep Sea Research Part II: Topical Studies in Oceanography*, *50*, 251–280. https://doi.org/10.1016/S0967-0645(02)00396-X

Veitch, J., Penven, P., & Shillington, F. (2009). The Benguela: A laboratory for comparative modeling studies. *Progress in Oceanography*, *83*, 296–302. https://doi.org/10.1016/j.pocean.2009.07.008

Weijer, W., de Ruijter, W. P. M., Dijkstra, H. A., & van Leeuwen, P. J. (1999). Impact of interbasin exchange on the Atlantic overturning circulation. *Journal of Physical Oceanography*, *29*, 2266–2284.

Weijer, W., Zharkov, V., Nof, D., Dijkstra, H. A., de Ruijter, W. P. M., Terwisscha van Scheltinga, A., et al. (2013). Agulhas ring formation as a barotropic instability of the retroflection. *Geophysical Research Letters*, *40*, 5435–5438. https://doi.org/10.1002/2013GL057751

Weiss, J. (1991). The dynamics of enstrophy transfer in two-dimensional hydrodynamics. *Physica D*, *48*(2–3), 273–294. https://doi.org/10.1016/0167-2789(91)90088-Q

Wells, N. C., Ivchenko, V. O., & Best, S. E. (2000). Instabilities in the Agulhas Retroflection Current system: A comparative model study. *Journal of Geophysical Research*, *105*, 3233–3241.

You, Y., Lutjeharms, J., Boebel, O., & de Ruijter, W. P. M. (2003). Quantification of the interocean exchange of intermediate water masses around southern Africa. *Deep Sea Research Part II: Topical Studies in Oceanography*, *50*(1), 197–228. https://doi.org/10.1016/S0967-0645(02)00384-3